LRP 815/06 March 2006

Final Report on Tests of advanced Nb_3Sn strands

EFDA reference: ASTEST contract 03-1121, Deliverable 4.3

R. Wesche, F. Roth, P. Bruzzone

ISSN 0458-5895

ÉCOLE POLYTECHNIQUE
FÉDÉRALE DE LAUSANNE

Final Report

Tests of Advanced Nb_3Sn Strands

EFDA Reference: ASTEST Contract 03-1121

Deliverable 4.3

Rainer Wesche, Felix Roth, and Pierluigi Bruzzone

Ecole Polytechnique Fédérale de Lausanne (EPFL)
Centre de Recherches en Physique des Plasmas
Association Euratom-Confédération Suisse
CH-5232 Villigen-PSI, Switzerland

February 2006

Centre de Recherches en Physique des Plasmas

Internal Report

Final Report on Tests of Advanced Nb_3Sn Strands

EFDA Reference: ASTEST Contract 03-1121

Deliverable 4.3

Rainer Wesche, Felix Roth, and Pierluigi Bruzzone

Ecole Polytechnique Fédérale de Lausanne (EPFL)
Centre de Recherches en Physique des Plasmas
Association Euratom-Confédération Suisse
CH-5232 Villigen-PSI, Switzerland

Table of Contents

1. Introduction

The observed performance drop in the large Nb_3Sn cable-in-conduit (CIC) conductors of the ITER model coils and short samples, likely due to transverse load degradation, lead to the definition of new design criteria for the optimisation of the Nb_3Sn conductors. In order to maintain the operational margins, "advanced" strands with higher critical current densities are required. In Japan and the United States high performance strands, optimised for fusion applications, have been developed and delivered to the KSTAR project in South Korea. To stimulate the European production capability for advanced Nb_3Sn strands prototype quantities of these strands have been ordered by the European industry. The advanced strands have been used for a complete characterisation of virgin strands. In addition, two short samples, TFAS1 and TFAS2, which are presently tested in SULTAN, have been fabricated of these high performance Nb_3Sn strands.

The suppliers of the advanced strands have performed acceptance tests on each strand unit length as a part of the quality assurance (QA) documentation provided to EFDA. Moreover, random cross-checking tests have been performed to verify the results from the suppliers. The results of the strand characterisation provide also a basis for the comparison of strand and short sample performances.

The objective of the present task is the measurement of the strand critical current, the residual resistivity ratio, and the copper to non-copper ratio of OST, EAS, and OCSI strands. The cross-checking tests have to verify whether the performance of the procured advanced strands (EFDA contract 03-953) is according the strand specification or not. In the present report, the results of the strand measurements, performed at CRPP, are described. To complete the picture the EAS and the OKSC witness strand results (from the heat treatment of TFAS1 and TFAS2 full size samples) are also presented in this report.

2. Experimental Details

2.1 Heat Treatment

The OST strands, used for the measurements at CRPP, have been heat treated together with the TFAS1 conductor under vacuum in the large Thermcraft tube furnace (see report of task SAMFSS). In the same heat treatment, the EAS witness strands A1-8930-6 and A1-8930-7 have been heat treated. Figure 2-1 shows the TFAS1 conductor, the OST and the EAS witness strands before insertion into the Thermcraft tube furnace. The OST and the EAS strands are wound onto Ti6Al4V ITER barrels.

A sketch of the heat treatment schedule for the TFAS1 conductor is shown in Figure 2-2. The TFAS1 heat treatment schedule is characteristic for internal tin Nb_3Sn strands. In the first annealing at 210°C, the tin is diffused into the copper surrounding the niobium filaments. The copper, required for the conductor stability, is protected by a tantalum barrier against in-diffusion of tin. During the first annealing step, the η- (60 weight percent tin, melting point 415°C) and the ε-phases (38 weight percent tin) are formed. In the further annealing steps at 340, 450 and 575°C the η-phase is converted to layers of the ε- and δ-phases (33 weight percent tin). The annealing temperatures are selected in such a way that no liquid phase is formed [1-3]. Finally, the tin diffuses at the highest temperature of 660°C from the copper-tin phases into the niobium filaments, which leads to the formation of the Nb_3Sn inter-metallic compound. The formation of the Nb_3Sn by inter-diffusion is a slow process, and hence long heat treatments are required.

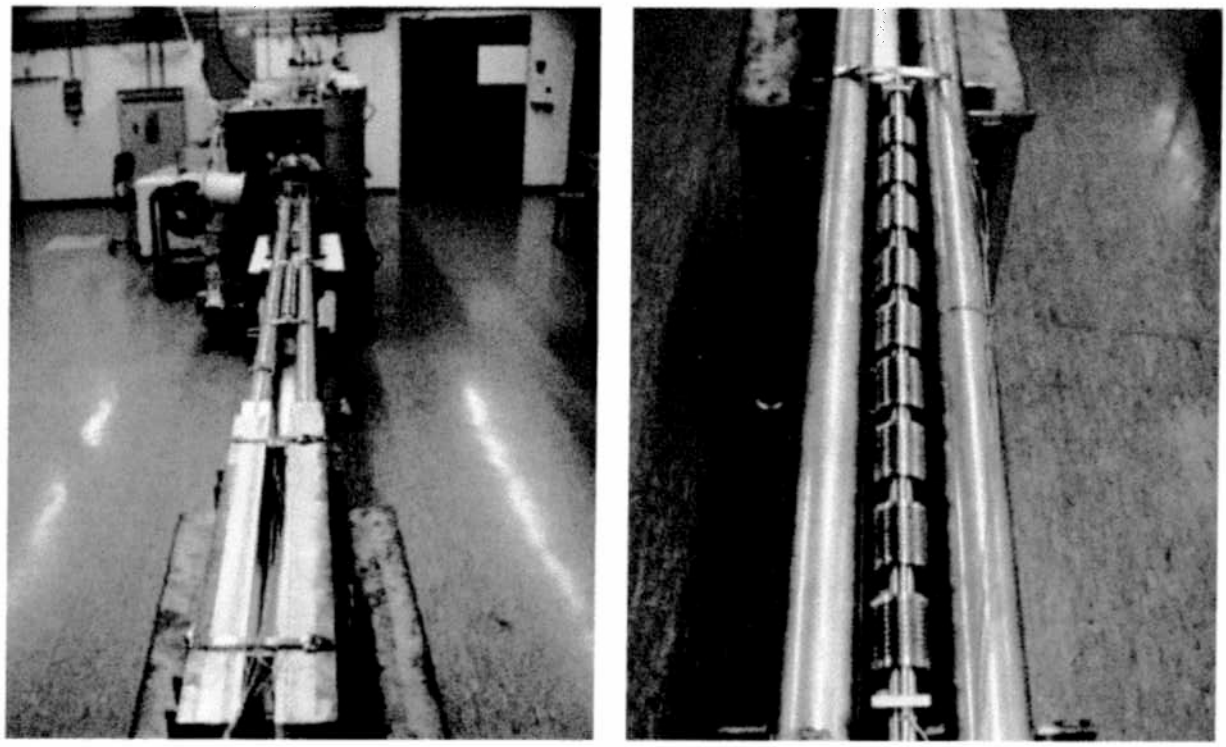

Figure 2-1. TFAS1 conductor (left) before insertion into the Thermcraft tube furnace. The OST and the EAS witness strands (right), which are heat treated together with the TFAS1 conductor, are wound onto Ti6Al4V ITER barrels. The barrels with the witness strands are placed in the central region of the furnace. The heat treatment is performed in vacuum.

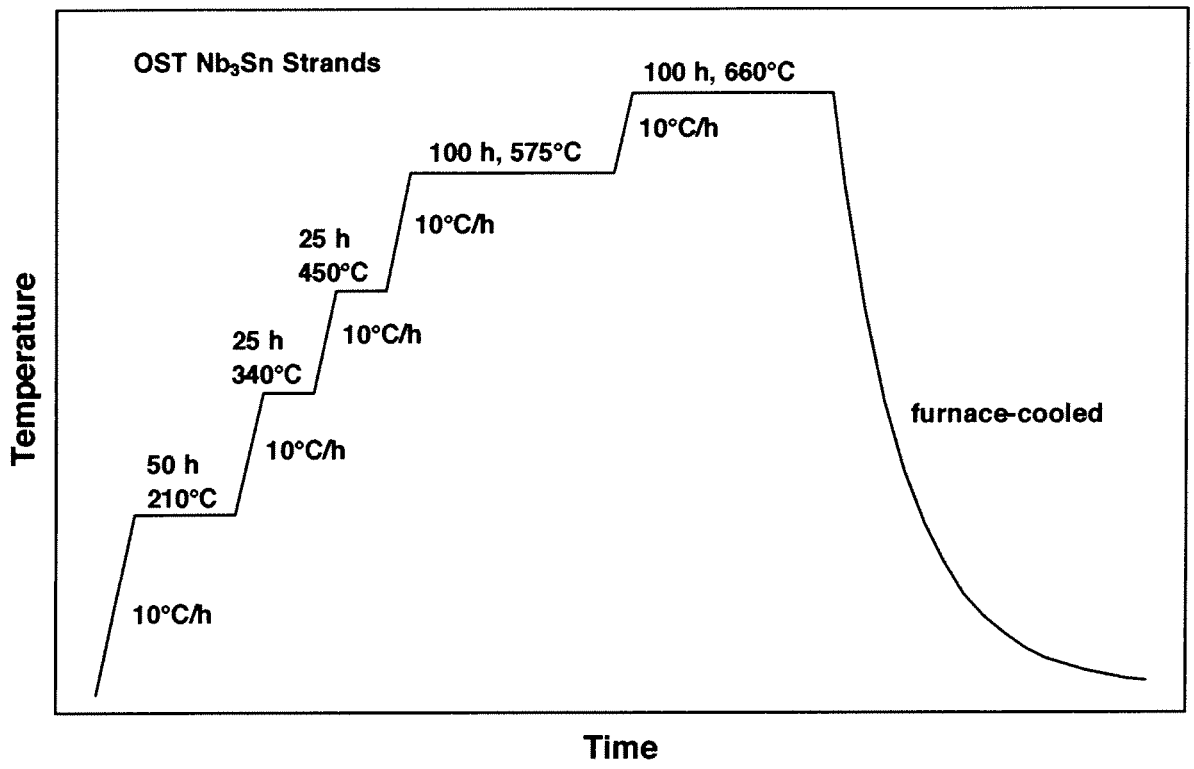

Figure 2-2. Sketch of the heat treatment schedule for the TFAS1 conductor, the OST and the EAS Nb_3Sn strands. The heat treatment has been performed in vacuum.

The EAS Nb_3Sn strands are fabricated by the bronze route. To reach the optimum performance a heat treatment schedule slightly different from that used for the TFAS1 conductor has to be used. Therefore, three EAS strands have been heat treated separately under argon atmosphere in the smaller Lenton tube furnace. A sketch of the heat treatment schedule is shown in Figure 2-3. In the bronze process, the amount of tin available for the formation of Nb_3Sn is limited by the solid solubility of tin in copper (≈13.5 weight percent tin). Due to the absence of phases rich in tin no annealing steps at 210, 340 and 450°C are required. The most important difference to the TFAS1 heat treatment is the much longer hold time at a slightly reduced maximum temperature of 620°C.

The other two Nb_3Sn strands OCSI and OKSC were procured by Outokumpu Italy and Outokumpu Finland, respectively. Both strands were heat treated together with the TFAS2 conductor in the Thermcraft tube furnace under vacuum. The heat treatment schedule is schematically illustrated in Figure 2-4 (the nominal duration of the step at 185°C has been extended from 24 to 32 h to account for the slow thermalization at low temperature, see report SAMFSS). The OCSI and the OKSC strands have been fabricated by the internal tin process. The heat treatment schedule, used for these strands and TFAS2, is therefore similar to the TFAS1 heat treatment schedule, shown in Figure 2-2.

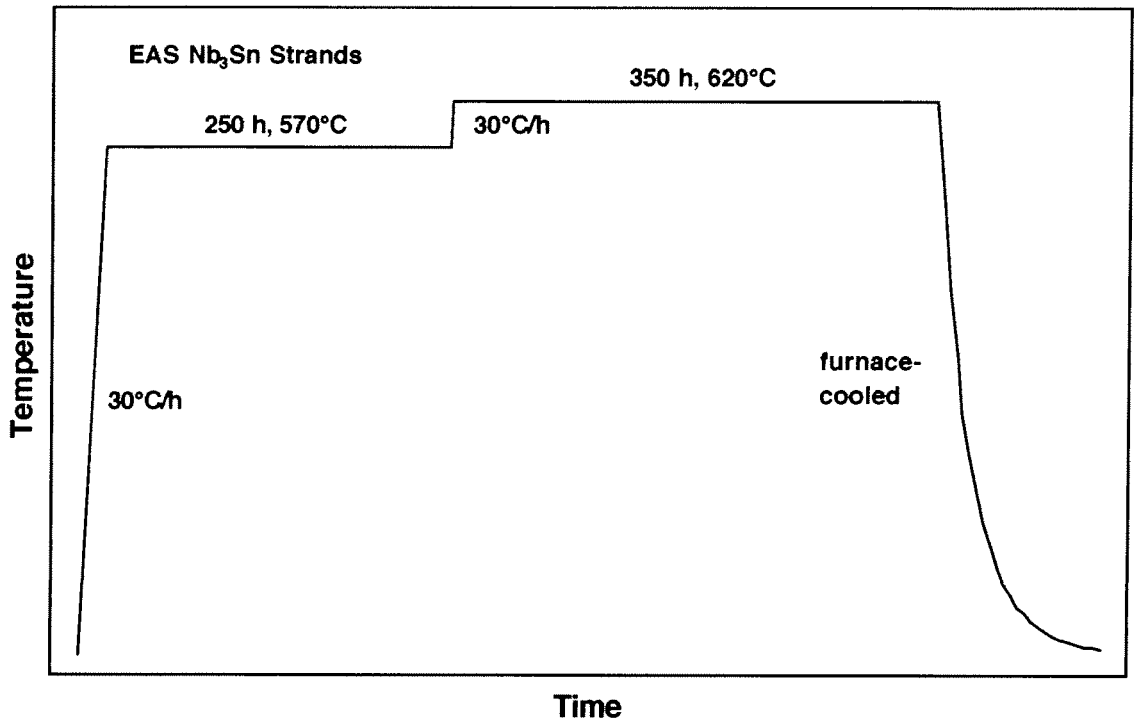

Figure 2-3. Sketch of the heat treatment schedule used for the EAS bronze route Nb_3Sn strands. The heat treatment has been performed under argon atmosphere in the small Lenton tube furnace.

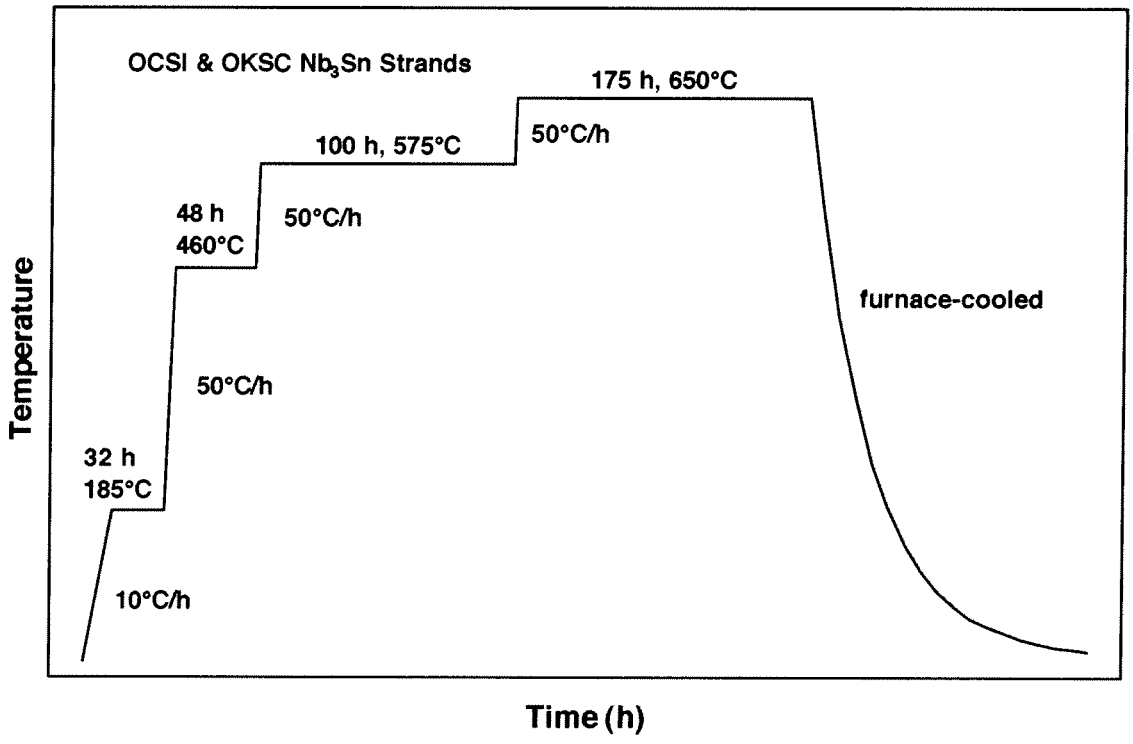

Figure 2-4. Sketch of the heat treatment schedule for the TFAS2 conductor, the OCSI and the OKSC Nb_3Sn strands. The heat treatment has been performed in vacuum.

2.2 Determination of the Copper to Non-Copper Ratio

The copper to non-copper ratio of the OST, EAS, and OCSI Nb_3Sn strands has been determined by an etching and weighing procedure. For each strand type, five sections of approximately 250 mm length have been used for the determination of the copper to non-copper ratio. The copper stabiliser is separated from the copper-tin alloy in the filament region by a tantalum diffusion barrier. The chromium coating is removed by etching with hydrochloric acid before the heat treatment. The weight, found before and after heat treatment, is nearly identical. After the heat treatment and the following weighing, the copper stabiliser is etched away using nitric acid. The filament region inside the tantalum diffusion barrier is not affected by the etching procedure. The difference of the weight, determined before and after etching of the copper stabiliser, provides the copper cross-section

$$A_{Cu} = \frac{m_{Cu}}{L\rho_{Cu}} \tag{1}$$

where m_{Cu} is the mass of the copper stabiliser, L the length of the strand section, and ρ_{Cu} = 8.92 g/cm^3 the density of copper. The ratio of copper to non-copper is

$$\frac{A_{Cu}}{A_{non-Cu}} = \frac{1}{\left(\frac{AL\rho_{Cu}}{m_{Cu}} - 1\right)} \tag{2}$$

where A is the calculated wire cross-section.

2.3 Measurement of the Residual Resistivity Ratio

The residual resistivity ratio for the Nb_3Sn strands is defined as

$$RRR = \frac{R(293K)}{R(\approx 18K)} \tag{3}$$

where R(293K) and R(≈18 K) are the resistances measured at room temperature and a temperature slightly above the transition temperature of Nb_3Sn ($T_c \cong$ 18.0 K). The voltage along the OST, EAS, and OCSI strands in the normal conducting state has been determined by the standard four-probe method. The measurements have been performed on short straight specimens of 10 cm length. The distance of the voltage taps is 30 mm. A temperature sensor is attached to the sample holder in the vicinity of the superconducting strand under test. The measurements at $T \approx$ 18 K have been performed in the cryostat of our 12 T laboratory magnet with the sample holder placed immediately above the liquid helium level. In the voltage measurements, the current has been ramped up with a rate of 0.1 A/s to a current level of a few amps. To study the effect of the chromium plating on the *RRR* one half of the strands has been heat treated with the chromium coating, while in the other half of the specimens the chromium coating has been removed before the heat treatment. The contribution of the tantalum barrier, the Nb_3Sn filaments and the surrounding copper-tin alloy to the normal state electrical conductivity is negligible.

2.4 Measurement of the Critical Current in Liquid Helium

The critical current of the Nb_3Sn strands has been measured by the standard four-probe method. An electric field criterion of 0.1 μV/cm has been used to define the critical current. For the measurement of the critical current at 4.2 K and fields between 8 and 12 T, the Nb_3Sn strands have been immersed in the liquid helium bath of our 12 T Nb_3Sn laboratory magnet. The critical current has been measured on the Ti6Al4V ITER barrels also used for the heat treatment of the strands. The distance of the voltage taps is 474 mm, i.e. the five central turns. The n value, defined by the expression $E = E_c(I/I_c)^n$ (E: electric field, E_c: = 0.1 μV/cm, I: current, I_c: critical current), has been determined in the electric field range of 0.1 to 1 μV/cm.

2.5 $I_c(B,T)$ Measurement Trials

Using a temperature-variable cryostat it has been tried to measure the critical current of the OST, EAS, OCSI, and OKSC Nb_3Sn strands at temperatures between 4.5 and 9 K in the field range of 8 to 12 T. The measurements have been again performed on the Ti6Al4V ITER barrels. To adjust the temperature to the desired value a heater is attached to the inner side of the ITER barrel (see Figure 2-5). The temperature is measured by a Cernox sensor attached to the outer central part of the ITER barrel (see Figure 2-5). The magneto-resistance of the Cernox sensor has been taken into consideration using the data in Reference [4]. The resulting corrections are listed in Table 2-1. Because of high critical currents up to 500 A, a considerable power is generated in the contacts and the current leads. To avoid an excessive thermal run away at the transition, the vacuum chamber of the temperature variable cryostat has to be filled with helium gas of a relatively high pressure. As a consequence there may result a considerable difference of the temperature measured in the centre of the ITER barrel and that present at the Nb_3Sn strand under test. To improve the thermal contact to the ITER barrel, the Nb_3Sn strands have been covered with silicon paste in some of the measurements. In other measurements a modified set-up has been used. In the modified set-up, a copper alloy sleeve surrounds the ITER barrel in order to avoid a direct thermal contact of the cold helium gas and the Nb_3Sn strand (see Figure 2-5). The copper alloy sleeve has been expected to be in good thermal contact with the ITER barrel. In these measurements, the Nb_3Sn strands have been not covered by silicon paste. The results, presented in Section 3.2, indicate that in the presently available set-up a relatively large systematic error in the measurement of the strand temperature cannot be avoided because of the high helium gas pressure required to remove the heat generated in the contacts and the current leads.

Table 2-1. Temperature corrections used to compensate the magneto-resistance of the Cernox sensor. The set points in the presence of an applied field are $T(B) = T - \Delta T(B,T)$, where T is the nominal temperature and $\Delta T(B,T)$ the required correction.

T(K)	ΔT(K)				
4.5	0.01	0.02	0.03	0.03	0.04
5.0	0.02	0.03	0.04	0.05	0.05
6.0	0.03	0.04	0.05	0.06	0.07
7.0	0.04	0.05	0.06	0.08	0.09
8.0	0.04	0.06	0.07	0.09	0.10
9.0	0.04	0.06	0.07	0.09	0.10
B(T)	8	9	10	11	12

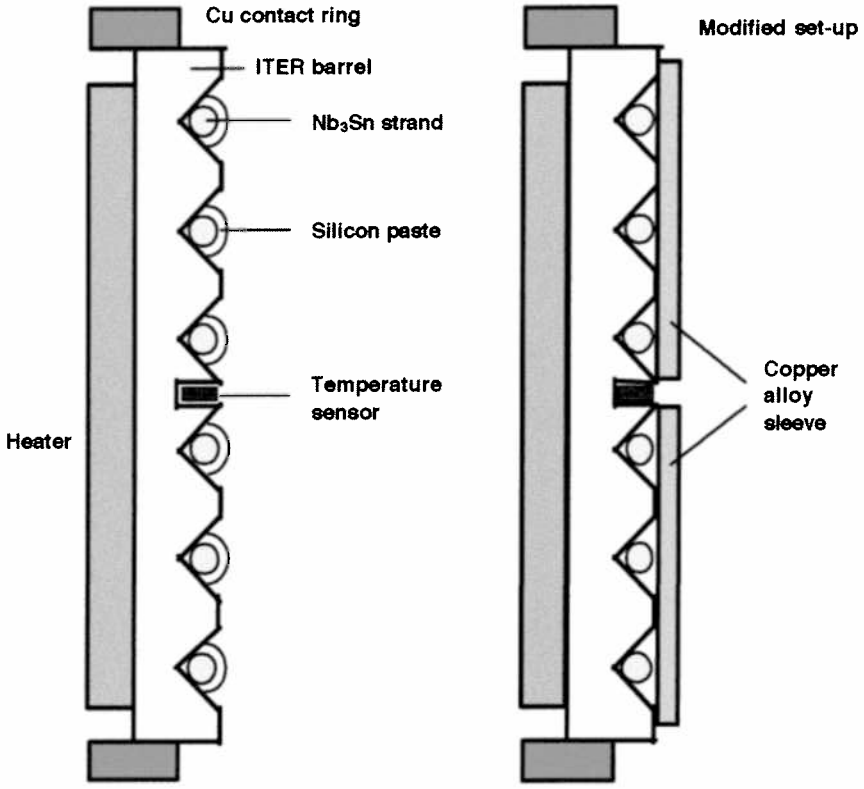

Figure 2-5. Sketch of the sample holder used for the $I_c(B,T)$ measurements.

3. Results

3.1 DC Performance at 4.2 K

3.1.1 OST Strands

First, the critical currents, found for the OST strands OST-7845-13, OST-7845-14, and OST-7845-15 at 4.2 K, are presented (the conductor TFAS1-OST sample was made out of 7845 strand billet). In Figure 3-1, the critical current of the OST strands is shown as a function of the applied magnetic field. The variation of the critical current of the three investigated specimens is 2.5 % at 8 T and 3.5 % at 12 T. The values measured at 4.2 K and 12 T are 273.2, 268, and 264 A for the specimens OST-13, Ost-14, and OST-15, respectively. The Cu : non-Cu ratio, found by an etching and weighing procedure, is 1.12 for the OST strands. Using a Cu : non-Cu ratio of 1.12 and the average critical current of 268.4 A for the three OST specimens, we find a non-copper critical current density of 1104 A/mm^2 at 4.2 K and 12 T. The critical current measured for specimens from the same billet at Oxford Superconductor Technology (OST) is 278 A (4.2 K, 12 T). The Cu : non-Cu ratio, expected by the supplier, is between 1.00 and 1.05 with a possible variation of 0.05 [5]. Thus, the Cu : non-Cu ratio of 1.12, measured at CRPP, is high but close to the upper limit of 1.1 expected to be possible by OST. Critical current measurements performed at ENEA provided a critical current of 273 A at 4.2 K and 12 T [5].

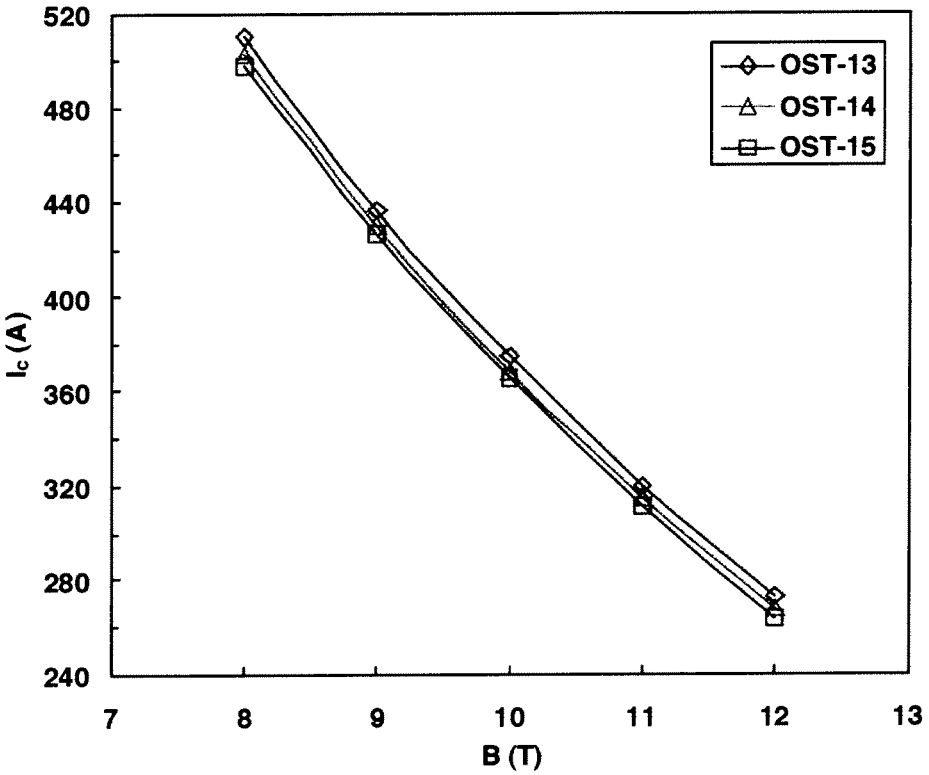

Figure 3-1. Critical current of the specimens OST-7845-13, OST-7845-14, and OST-7845-15 as a function of the applied magnetic field at 4.2 K. Depending on the applied magnetic field the scatter in the critical current of the three OST specimens varies between 2.5 and 3.5 %.

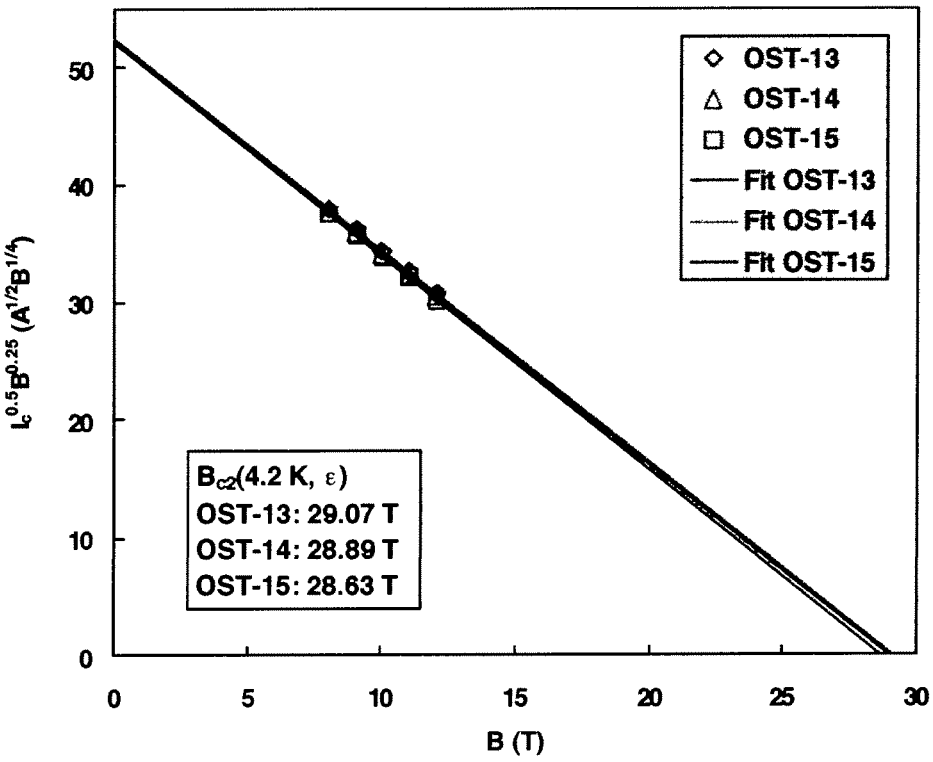

Figure 3-2. Kramer plots for the specimens OST-13, OST-14 and OST-15 providing upper critical fields between 28.63 and 29.07 T at 4.2 K.

The pinning force density (F_p) in Nb_3Sn superconductors can be well described by the scaling relation [6]

$$F_p = |\mathbf{j}_c \times \mathbf{B}| \propto b^{0.5}(1-b)^2 \tag{4}$$

where $b = B/B_{c2}(\varepsilon,T)$. The upper critical field of Nb_3Sn depends on the strain and the temperature. Summers et al. [7] proposed for the critical current of Nb_3Sn superconductors the following scaling relation

$$I_c(B,T,\varepsilon) = C(\varepsilon)(B_{c2}(T,\varepsilon))^{-0.5}(1-t^2)^2 b^{-0.5}(1-b)^2 \tag{5}$$

where $C(\varepsilon)$ is a coefficient independent of field and temperature and $t = T/T_c(\varepsilon)$. The upper critical field can be expressed as

$$B_{c2}(T,\varepsilon) = B_{c20}(\varepsilon)(1-t^2)[1-0.31t^2(1-1.77\ln t)] \tag{6}$$

Rearrangement of Equation (5) leads to the expression

$$I_c^{0.5}B^{0.25} = C(\varepsilon)^{0.5}(1-t^2)\left(1-\frac{B}{B_{c2}(T,\varepsilon)}\right) = K(T,\varepsilon)\left(1-\frac{B}{B_{c2}(T,\varepsilon)}\right) \tag{7}$$

Equation (7) indicates that a Kramer plot of $I_c^{0.5}B^{0.25}$ versus B provides an estimation of the upper critical field at the temperature T. Figure 3-2 shows a Kramer plot for the critical current data of the OST strands. The estimated upper critical field at 4.2 K and strain according to the sample holder varies between 28.63 and 29.07 T.

3.1.2 EAS Strands

Two different heat treatments have been performed for the EAS Nb_3Sn strands. The long heat treatment (see Figure 2-3), optimized for this bronze route conductor, has been used for the specimens A1-8930-3 (EAS-3), A1-8930-4 (EAS-4), and A1-8930-5 (EAS-5), while specimens A1-8930-6 (EAS-6) and A1-8930-7 (EAS-7) have been heat treated together with the TFAS1 conductor (see Figure 2-2). The critical current as a function of the applied magnetic is shown for both groups of EAS Nb_3Sn specimens in Figure 3-3. The scatter in the critical current data, measured at 4.2 K, is around 2 % for the long heat treatment, performed in the small Lenton tube furnace under argon atmosphere. For the witness strands (EAS-6, EAS-7), which have been heat treated together with the TFAS1 conductor, the difference of the critical currents at 4.2 K is less than 1 %. At CRPP a Cu : non-Cu ratio of 0.93 has been determined for the EAS strands. This Cu : non-Cu ratio is nearly identical to the value of 0.92 expected from the data provided by European Advanced Superconductors (EAS) [5]. Using the Cu : non-Cu ratio of 0.93 and the average critical current of 215.7 A (EAS-3, EAS-4, EAS-5), we find a critical current density of 808 A/mm^2 at 4.2 K and 12 T.

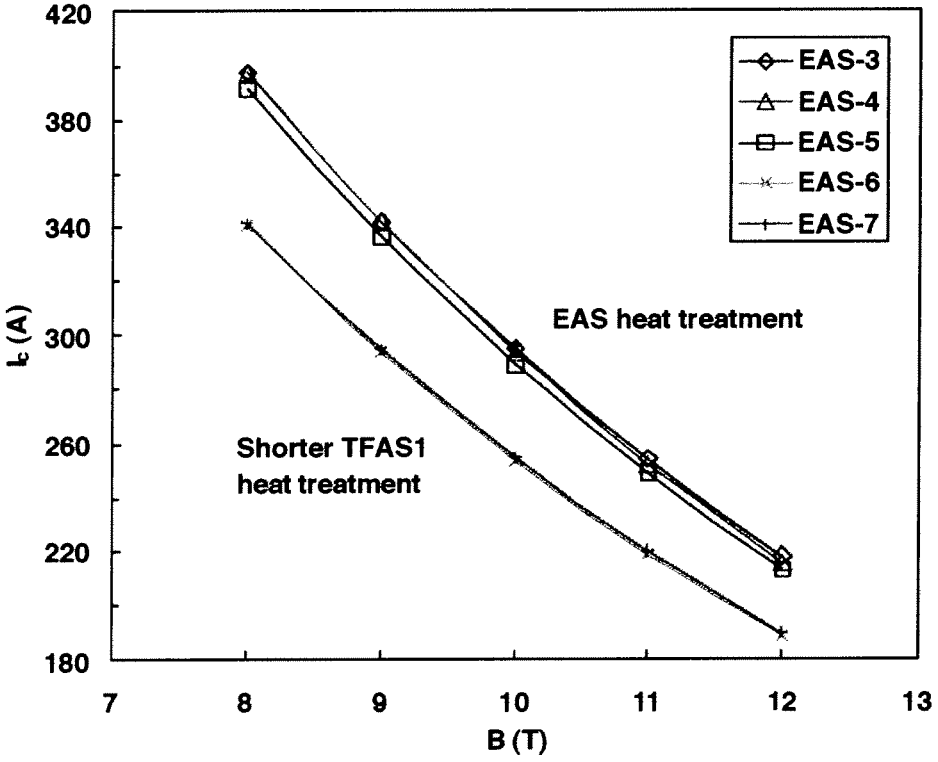

Figure 3-3. Critical current of the EAS strands as a function of applied field at 4.2 K. The long heat treatment, optimised for this bronze route strand, has been used for the specimens EAS-3, EAS-4 and EAS-5. The other two specimens have been heat treated together with the TFAS1 conductor.

For the witness strands (EAS-6, EAS-7) the average critical current is 189.2 A at 4.2 K and 12 T (non-copper critical current density of 709 A/mm^2). The shorter heat treatment of the witness strands leads to a 12 % reduction of the critical current at 4.2 K and 12 T. Critical currents between 188 and 190 A have been measured at the Forschungszentrum Karlsruhe for EAS specimens subjected to the same heat treatment schedule than that used for the TFAS1 conductor [5].

The Kramer plots for both groups of EAS strands are shown in Figure 3-4. For the long heat treatment (EAS-3, 4, 5), upper critical fields between 29.65 and 30.23 T have been found at 4.2 K. Even slightly higher upper critical fields between 30.66 and 30.85 T have been determined for the EAS strands heat treated together with the TFAS1 conductor.

3.1.3 OCSI Strands

Figure 3-5 shows the critical current of the specimens OCSI 1, OCSI 2, and OCSI-3 as a function of the applied magnetic field at 4.2 K. The scatter in the critical current data is around 3 %. The average critical current of the three specimens is 210.5 A at 4.2 K and 12 T. By means of a weighing and etching procedure a Cu : non-Cu ratio of 1.52 has been determined at CRPP (1.45 according to the supplier [5]). The resulting average non-copper critical current density is 1029 A/mm^2 at 4.2 K and 12 T. At the moment, there are no other measurements available for the OCSI strands subjected to the TFAS2 heat treatment (see Figure 2-4).

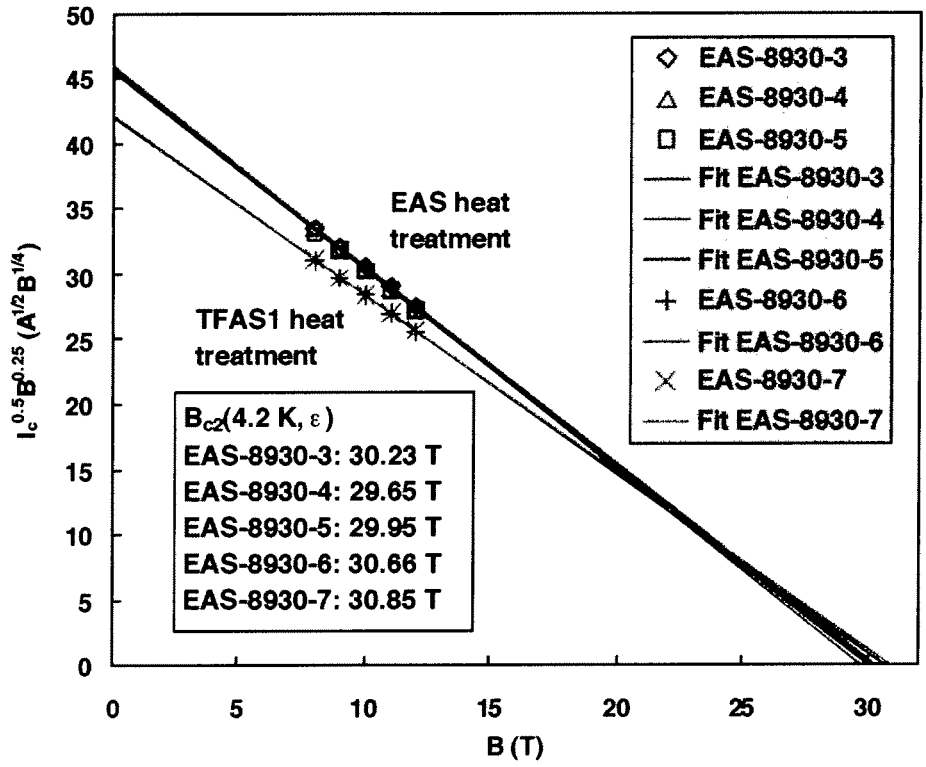

Figure 3-4. Kramer plots for the EAS strands heat treated in the Lenton tube furnace (long heat treatment, EAS-3, 4, 5) and the witness strands (EAS-6, 7) heat treated together with the TFAS1 conductor.

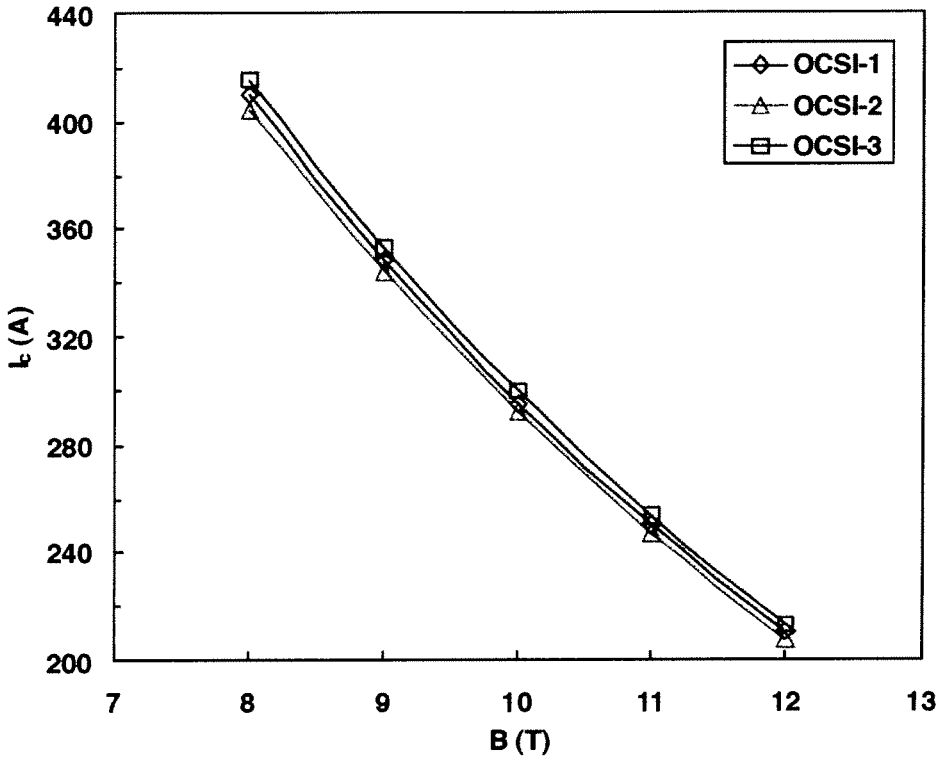

Figure 3-5. Critical current of the OCSI strands as a function of applied field at 4.2 K.

In Figure 3-6, the Kramer plots for the specimens OCSI-1, OCSI-2, and OCSI-3 are shown. The estimated upper critical field is between 27.29 and 27.38 T at 4.2 K. The variation in the upper critical field is less than 0.1 T.

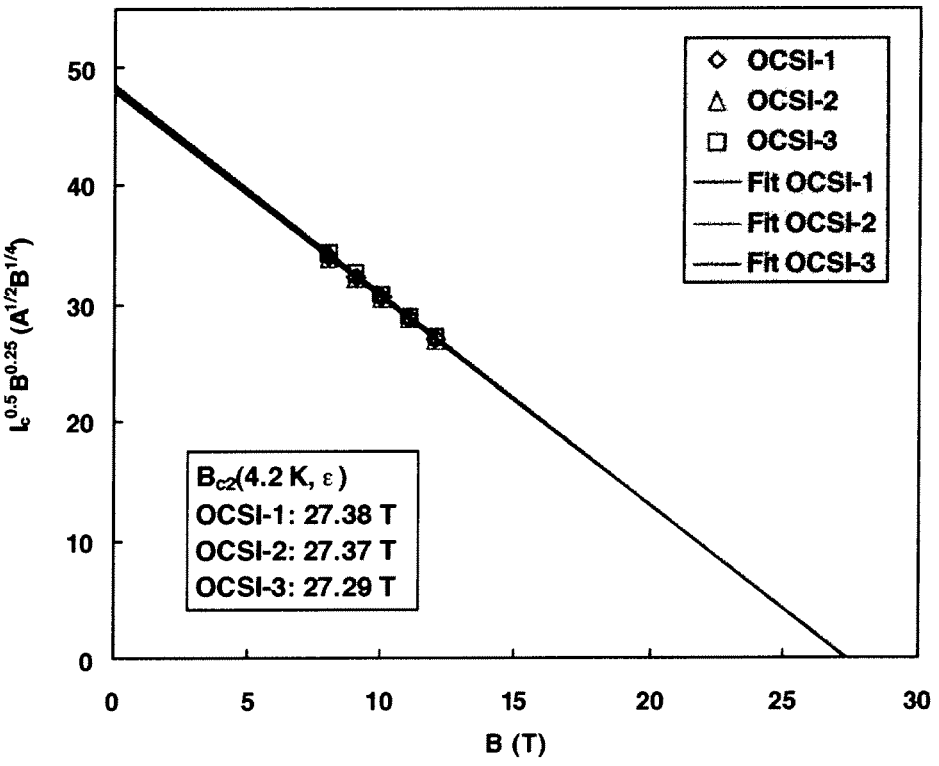

Figure 3-6. Kramer plots for the specimens OCSI-1, OCSI-2 and OCSI-3 providing upper critical fields between 27.29 and 27.38 T at 4.2 K.

3.1.4 OKSC Strands

The critical current data for the OKSC strands, heat treated together with the TFAS2 conductor, are shown in Figure 3-7. The critical current of OKSC-7 is 5 % higher than that of OKSC-6. The critical currents at 4.2 K and 12 T for OKSC-6 and OKSC-7 are 244.4 and 257.7 A, respectively. The Cu : non-Cu ratio of this strand has not been measured at CRPP. Using the average critical current of 251 A and the Cu : non-Cu ratio of 1.0, obtained by CEA [5], we find a non-copper critical current density of 974 A/mm^2 at 4.2 K and 12 T.

The Kramer plots for the two OKSC specimens are shown in Figure 3-8. An upper critical field between 28.60 and 28.92 T at 4.2 K has been estimated from the Kramer plot.

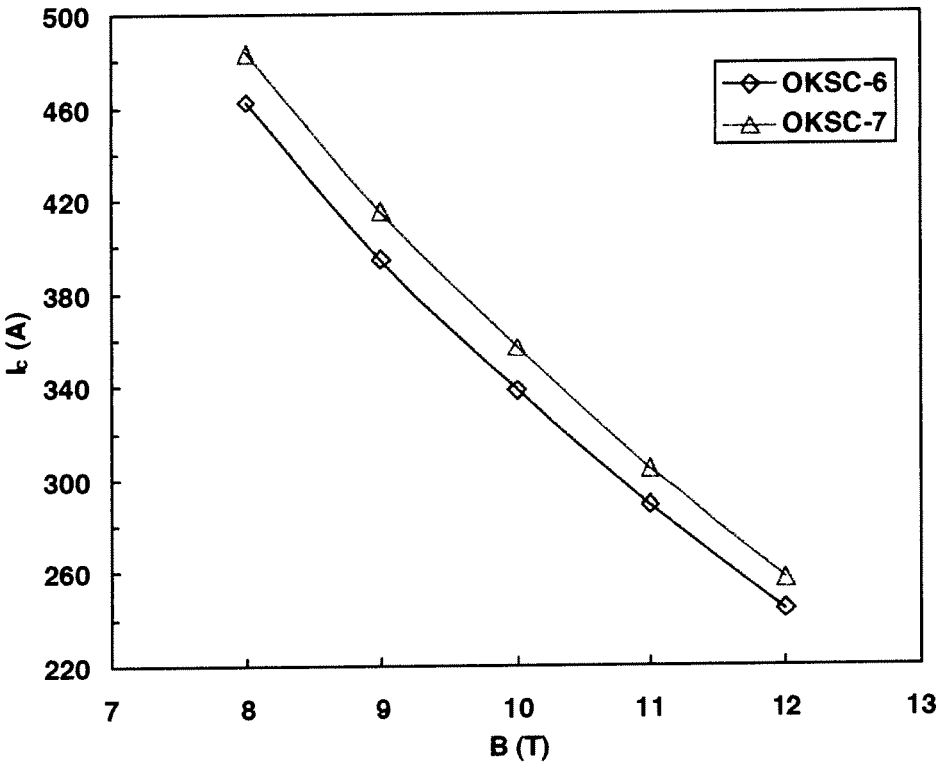

Figure 3-7. Critical current of the OKSC strands as a function of applied field at 4.2 K.

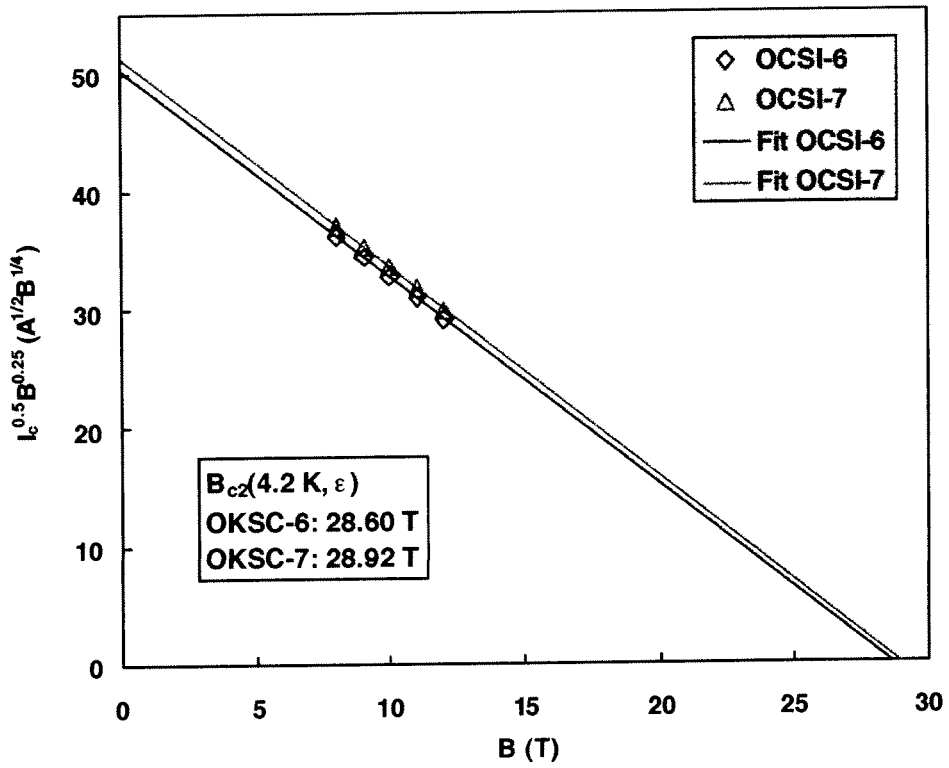

Figure 3-8. Kramer plots for the specimens OKSC-6 and OKSC-7 providing upper critical fields between 28.60 and 28.92 T at 4.2 K.

3.2 Problems in the Measurement of $I_c(B,T)$

In the measurements of the critical current of the advanced Nb_3Sn strands, the main problems encountered are the weak thermal contact of the Nb_3Sn strand and the ITER barrel and the heat generation in the sample holder (contacts and current leads). The temperature sensor used to adjust the strand temperature is in good thermal contact with the central outer part of the ITER barrel (see Figure 2-5). On the one hand, a high pressure of the helium gas in the vacuum chamber of the temperature variable cryostat is required to remove the generated heat. On the other hand, a large temperature difference between the superconducting strand under test and the ITER barrel may be required to establish a balance of the heat conduction from the barrel to the strand and the heat transfer from the strand to the cold helium gas (see Figure 2-5). To improve the thermal contact of the strand and the ITER barrel, the strands have been covered with silicon paste in some of the measurements. The disadvantage of the use of silicon paste is a changed strain state of the Nb_3Sn strands. Figure 3-9 shows the critical current of EAS-3 and OST-13 measured in liquid helium with and without silicon paste. For the EAS strands, the effect of the silicon paste on the critical current is negligibly small. However, a 2 % enhancement of the critical current has been found for the OST strand covered with silicon paste.

In other measurements, the ITER barrel has been covered by a copper alloy sleeve protecting the Nb_3Sn strand from a direct contact with the cold helium gas (see Figure 2-5). In these measurements, the Nb_3Sn strands have been not covered by silicon paste. Supposing a relatively good thermal contact of the copper alloy sleeve and the ITER barrel a reasonably good agreement of strand and barrel temperature may be expected. The results of the I_c measurements in the temperature variable cryostat suggest that the use of a copper alloy cover is not sufficient to ensure a negligible difference of the temperatures of the strand and the barrel.

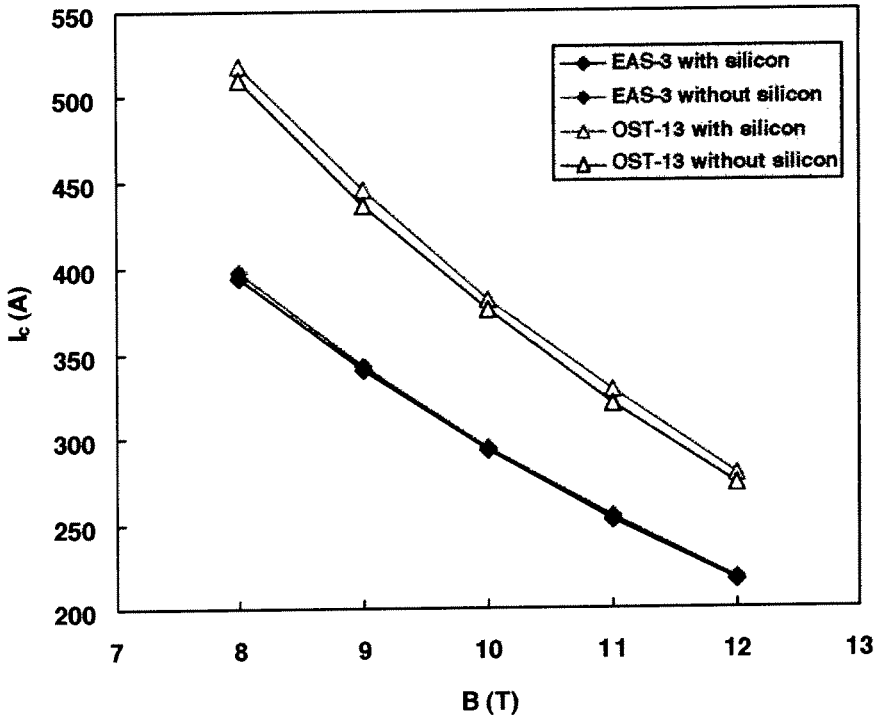

Figure 3-9. Critical current of the specimens EAS-3 and OST-15 measured in liquid helium with and without silicon paste.

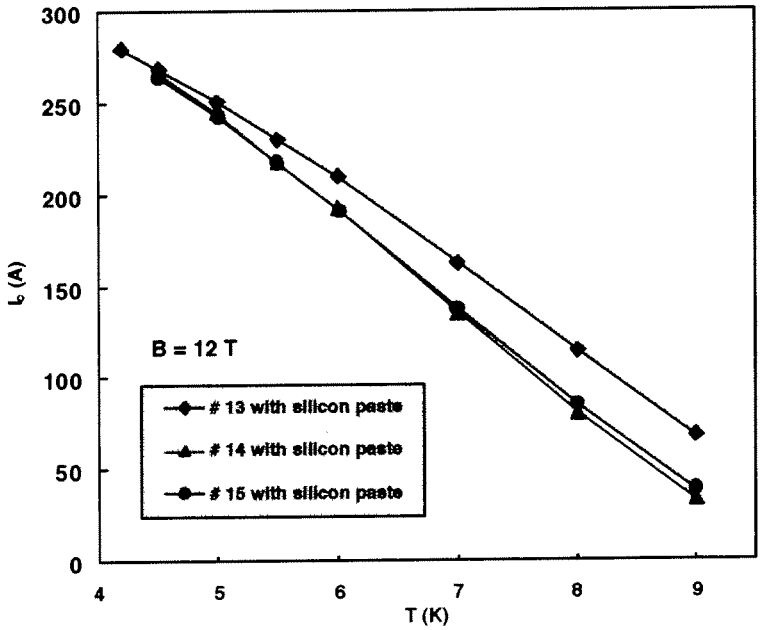

Figure 3-10. Scatter of the critical current of the specimens OST 13, 14, and 15 for measurements with silicon paste.

A first evidence for a systematic error in the measurement of the strand temperature is the large scatter in the critical current at 12 T and 9 K for the three OST specimens with nearly identical critical currents at 4.2 K. This behavior is illustrated in Figures 3-10 and 3-11 for measurements with silicon paste and in the modified set-up (additional copper alloy sleeve), respectively. A further indication of an underestimation of the strand temperature is the critical current measured at 4.5 K in the modified set-up. For the specimens OST 14 and 15, the critical current at a nominal temperature of 4.5 K is as high as the value obtained at 4.2 K.

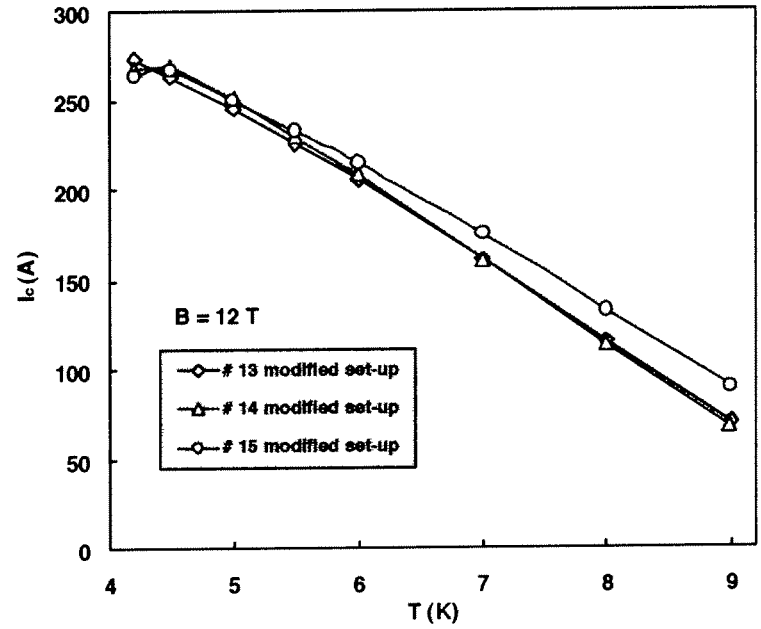

Figure 3-11. Scatter of the critical current of the specimens OST 13, 14, and 15 for measurements in the modified set-up without silicon paste.

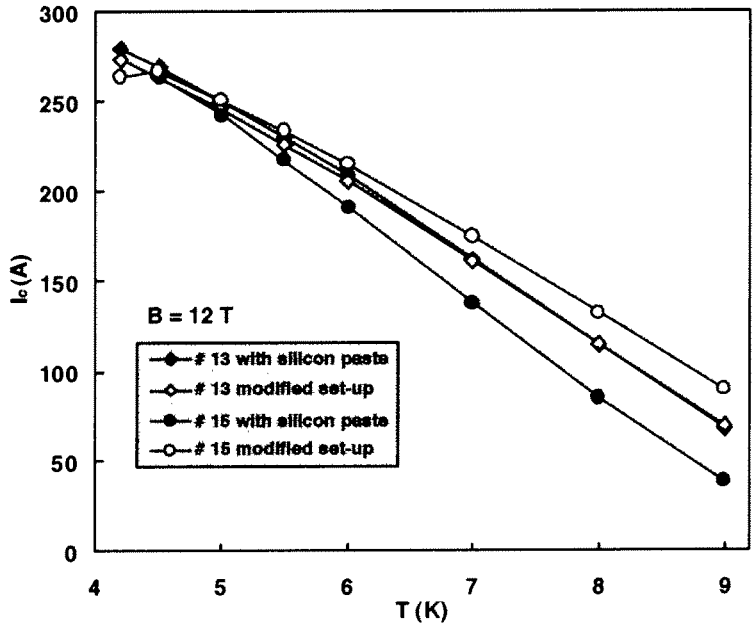

Figure 3-12. Comparison of the critical currents of the specimens OST-13 and OST-15 measured at 12 T with silicon paste and in the modified set-up.

In Figure 3-12, the critical currents at 12 T measured with silicon paste and in the modified set-up are compared. For the specimen OST-13, both measurements provide nearly identical critical currents, whereas a large difference in the measured I_c values has been found for the specimen OST-15. In the case of OST-15 for both types of measurements the critical current at 4.5 K is overestimated. The large difference in the critical current of OST-15 obtained for the two different measurement procedures reflects a large systematic error in the conductor temperature, which may reach values up to 1 K. The results for OST-13 have been retained (see Figure 3-20).

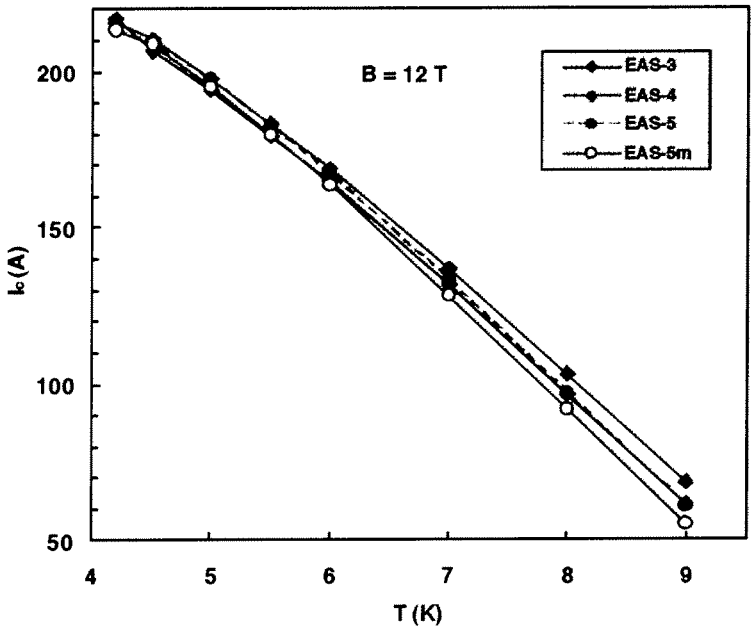

Figure 3-13. Scatter of the critical current of the specimens EAS-3, 4, and 5 for measurements with silicon paste. For EAS-5 also the data obtained in the modified set-up are shown (EAS-5m).

Figure 3-13 shows the scatter in the critical currents of the specimens EAS-3, EAS-4, and EAS-5, subjected to the long heat treatment (see Figure 2-3). For the specimen EAS-5, the results of the measurements with silicon paste and in the modified set-up are also compared in Figure 3-13. In this case the critical currents measured at 12 T in the modified set-up are lower than the values found for the silicon paste coated strand. This is the opposite behavior than that observed for the specimen OST-15 (see Figure 3-12).

The critical currents of the silicon paste coated strands EAS-6 and EAS-7 (witness strands) measured at 12 T are compared in Figure 3-14. The specimens EAS-6 and EAS-7 have been heat treated together with the TFAS1 conductor. The difference of the critical currents at elevated temperatures seems to be again mainly caused by a systematic error in the conductor temperature.

In order to estimate the systematic error in the strand temperature, Kramer plots and Summers fits have been used. In Figures 3-15 and 3-16, the Kramer plots for EAS-7 and OCSI-1-2-3 (average critical currents of OCSI-1, 2, 3) are shown, respectively. In the Kramer plots for OCSI-1-2-3, the data points for all temperatures and fields are close to the linear fit lines. In contrast to this behavior, Figure 3-15 clearly shows that for temperatures of 8 and 9 K the 8 T data points deviate from the linear fit. This result indicates that the strand temperature at 8 T, i.e. the highest current, is higher than those at the higher fields. Such a current dependent error in the strand temperature leads to an incorrect slope of the straight lines in the Kramer plots. The Kramer plots provide $B_{c2}(T,\varepsilon)$ and $K(T,\varepsilon) = C(\varepsilon)^{0.5}(1-(T/T_c(\varepsilon))^2)$, where $C(\varepsilon)$ is a factor independent of temperature (see Equation (7)). The temperature dependence of the upper critical field at constant strain is given by Equation (6). Using the values of $B_{c2}(T,\varepsilon)$ and $K(T,\varepsilon)$ provided by the Kramer plots as well as the corresponding temperature dependencies, the critical temperature can be determined independently from the B_{c2} and the K data sets. The difference in the $T_c(\varepsilon)$ values, derived from the two data sets, is a measure of the current dependent systematic error of the strand temperature.

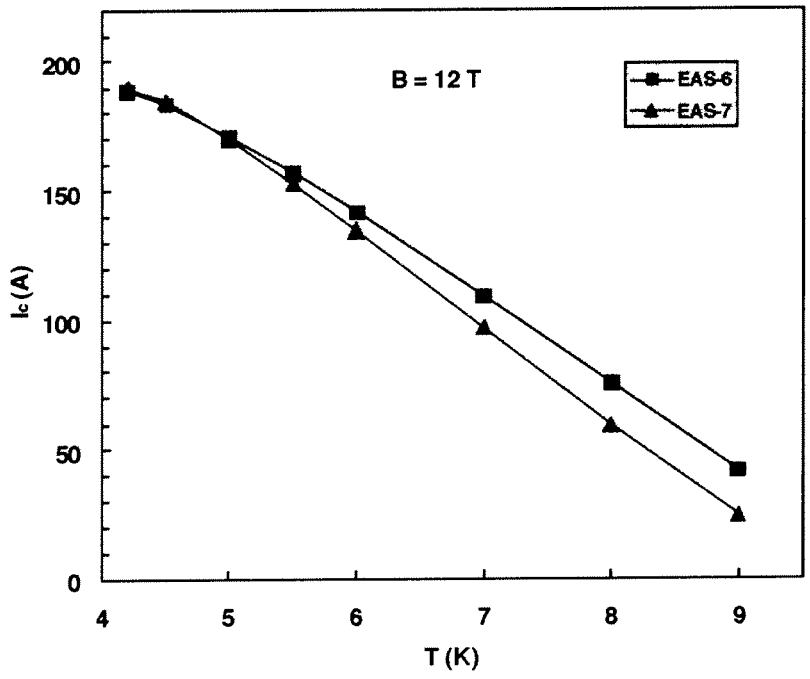

Figure 3-14. Comparison of the critical currents of the specimens EAS-6 and EAS-7 (TFAS1 heat treatment) measured at 12 T with silicon paste.

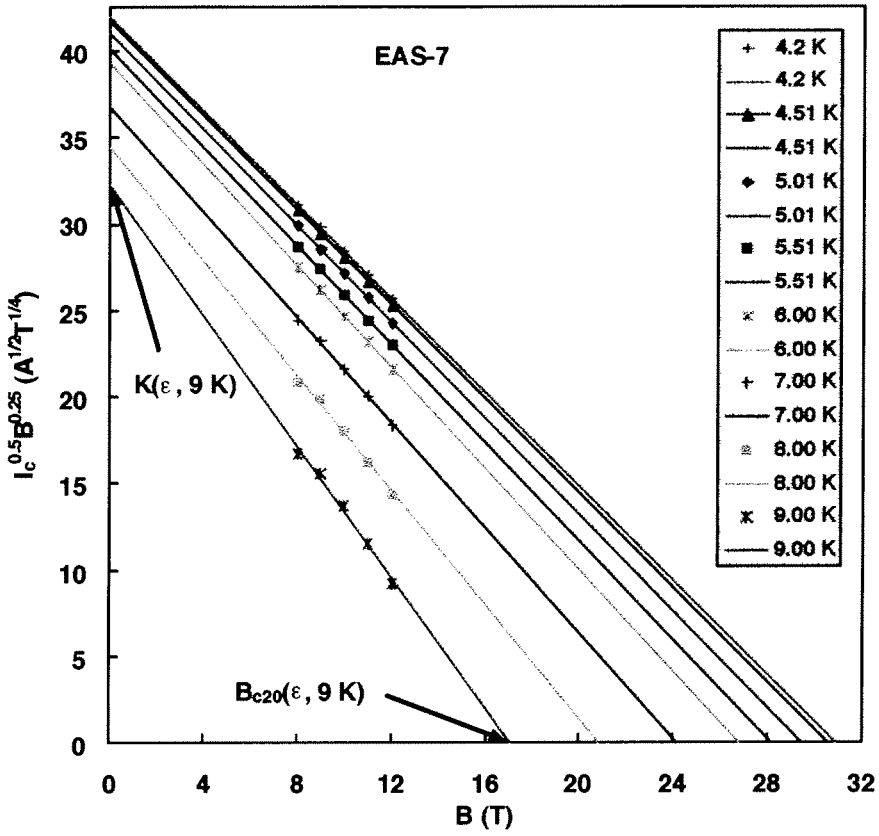

Figure 3-15. Kramer plots for the specimen EAS-7.

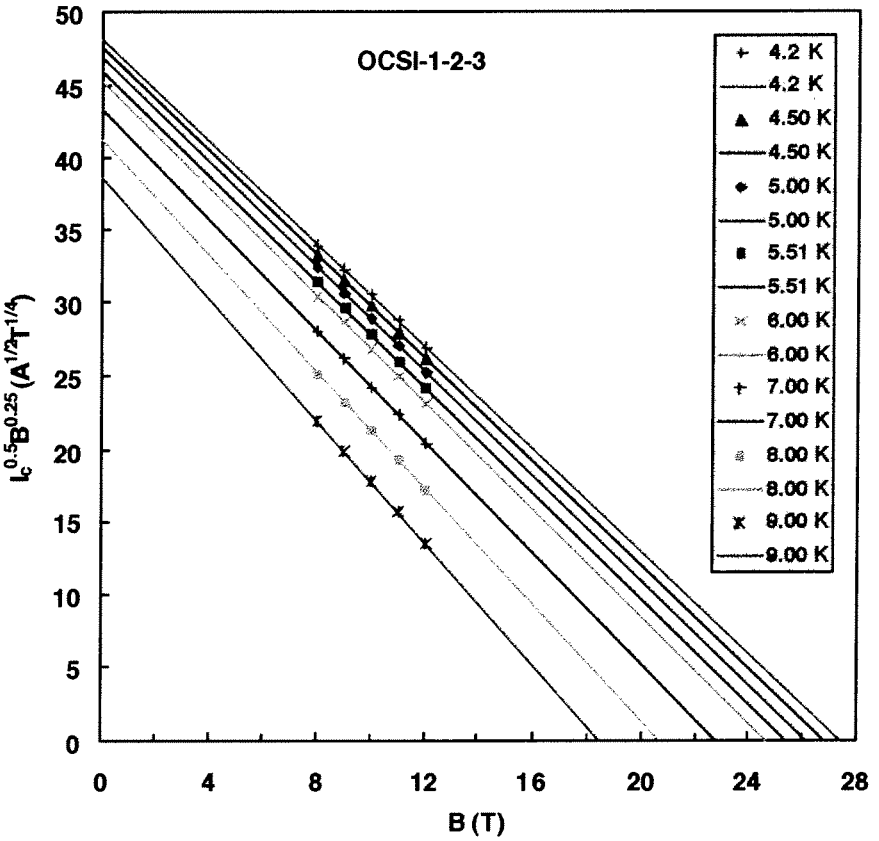

Figure 3-16. Kramer plots for the average critical currents of OCSI-1, 2, and 3.

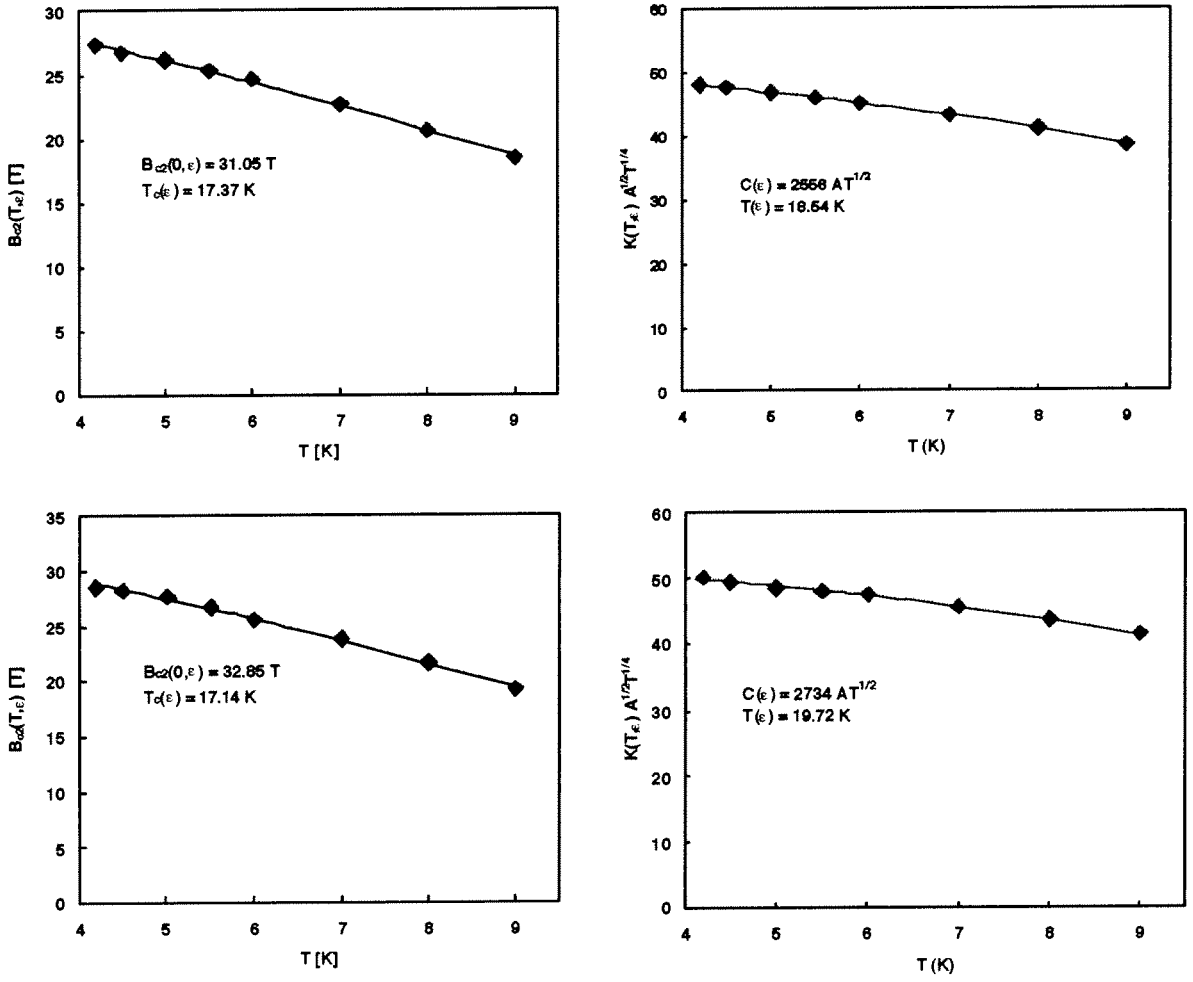

Figure 3-17. $B_{c2}(T,\varepsilon)$- and $K(T,\varepsilon)$-fits for OCSI-1-2-3 (top) and EAS-7 (bottom) obtained from the data provided by the Kramer plots shown in Figures 3-15 and 3-16.

Figure 3-17 shows examples of $B_{c2}(T,\varepsilon)$- and $K(T,\varepsilon)$-fits. For the OCSI strands (Figure 3-17 top) a moderate difference of the critical temperatures obtained by the two fits ΔT_c = 18.54 K – 17.37 K = 1.17 K has been obtained. A much larger ΔT_c of 2.58 K has been found for EAS-7 (Figure 3-17 bottom). The results of the B_{c2}- and K-fits are summarized in Table 3-1. For temperatures around 6 K (≈1/3 $T_c(Nb_3Sn)$) the systematic error in the strand temperature is estimated to be $\Delta T = \pm(1/2)(1/3)(T_c(\varepsilon)(K\text{-fit})-T_c(\varepsilon)(B_{c2}\text{-fit}))$.

Furthermore, Summers fits, based on Equations (5) and (6), have been performed for all data sets. The results of the Summers fits are gathered in Table 3-2. The critical temperature $T_c(\varepsilon)$, found from the Summers fits, is between the extreme values obtained from the Kramer plot based $B_{c2}(T,\varepsilon)$- and $K(T,\varepsilon)$-fits. For most of the measurements, the Summers fit line deviates considerably from the measured critical current at 4.2 K. These differences ΔT(Fit/4.2 K data) reflect again a systematic error in the measurement of the strand temperature. We suppose that the total uncertainty in the measured strand temperature is

$$\Delta T = \pm\left(\Delta T(\text{Fit/4.2 K data}) + \frac{1}{6}\left(T_c(\varepsilon)\{\text{K fit}\} - T_c(\varepsilon)\{B_{c2}\text{ fit}\}\right)\right) \tag{8}$$

Table 3-1. Results of $B_{c2}(T,\varepsilon)$ and $K(T,\varepsilon)$-fits.

Specimen	$B_{c20}(\varepsilon)$ [T]	$T_c(\varepsilon)$ [K]	$C(\varepsilon)$ [AT$^{1/2}$]	$T_c(\varepsilon)$ [K]	ΔT_c [K]
OST-13 with silicon paste	34.26	16.18	3057	18.70	2.52
OST-13 modified set-up	33.91	16.43	3005	18.99	2.56
OST-14 with silicon paste	34.75	14.76	3281	15.61	0.85
OST-14 modified set-up	34.33	16.12	3004	19.09	2.97
OST-15 with silicon paste	34.63	15.13	3209	15.86	0.73
OST-15 modified set-up	33.13	18.01	2965	19.99	1.98
EAS-3 with silicon paste	34.66	16.94	2224	20.75	3.81
EAS-4 with silicon paste	34.33	17.16	2286	20.02	2.86
EAS-5 with silicon paste	34.94	16.54	2263	19.62	3.08
EAS-5 modified set-up	35.12	16.23	2277	18.75	2.52
EAS-6 with silicon paste	36.43	15.42	1954	18.53	3.11
EAS-7 with silicon paste	37.45	14.29	2018	16.75	2.46
OCSI-1-2-3 modified set-up	31.05	17.37	2556	18.54	1.17
OKSC-6 modified set-up	32.85	17.14	2734	19.72	2.58

Table 3-2. Results of the Summers fits.

Specimen	$T_c(\varepsilon)$ [K]	$C(\varepsilon)$ [AT$^{1/2}$]	$B_{c20}(\varepsilon)$ [T]	ΔT(Fit/4.2 K data) [K]
OST-13 with silicon paste	17.33	3162	33.21	0.06
OST-13 modified set-up	17.58	3108	32.91	0.06
OST-14 with silicon paste	15.27	3303	34.30	0.20
OST-14 modified set-up	17.45	3127	33.10	0.26
OST-15 with silicon paste	15.58	3221	34.26	0.18
OST-15 modified set-up	18.92	3025	32.57	0.28
EAS-3 with silicon paste	17.90	2332	33.77	0.02
EAS-4 with silicon paste	18.47	2362	33.27	0.08
EAS-5 with silicon paste	17.96	2351	33.68	0.16
EAS-5 modified set-up	17.40	2356	34.02	0.14
EAS-6 with silicon paste	16.79	2048	34.92	0.13
EAS-7 with silicon paste	15.34	2109	36.12	0.17
OCSI-1-2-3 modified set-up	17.90	2591	30.72	0.05
OKSC-6 modified set-up	18.27	2815	32.03	0.00

Using the slopes of the fit lines (B = 10 T, 6 K ≤ T ≤ 7 K) provided by the Summers fits and the estimated error in the strand temperature the expected error in the critical current has been calculated. The expected errors in the strand temperature and critical current are listed in Table 3-3.

In Figure 3-18, the scatter in the critical current data (B = 10 T) of OST-13 (modified set-up), OST-14 (with silicon paste), and OST-15 (modified set-up) are compared. The error bars estimated in Table 3-3 are also included. The error bars for the specimens with the highest and lowest measured critical current overlap at temperatures of 7 K and below. The extreme differences in I_c are slightly larger than the sum of the error bars at the highest temperatures of 8 and 9 K.

Table 3-3. Errors in the strand temperature and critical current estimated from the data in Tables 3-1 and 3-2.

Specimen	ΔT [K]	ΔI_c [A]
OST-13 with silicon paste	±0.48	±26
OST-13 modified set-up	±0.49	±26
OST-14 with silicon paste	±0.34	±23
OST-14 modified set-up	±0.76	±40
OST-15 with silicon paste	±0.30	±19
OST-15 modified set-up	±0.61	±29
EAS-3 with silicon paste	±0.66	±26
EAS-4 with silicon paste	±0.56	±22
EAS-5 with silicon paste	±0.67	±27
EAS-5 modified set-up	±0.56	±24
EAS-6 with silicon paste	±0.65	±25
EAS-7 with silicon paste	±0.58	±26
OCSI-1-2-3 modified set-up	±0.25	±11
OKSC-6 modified set-up	±0.43	±19

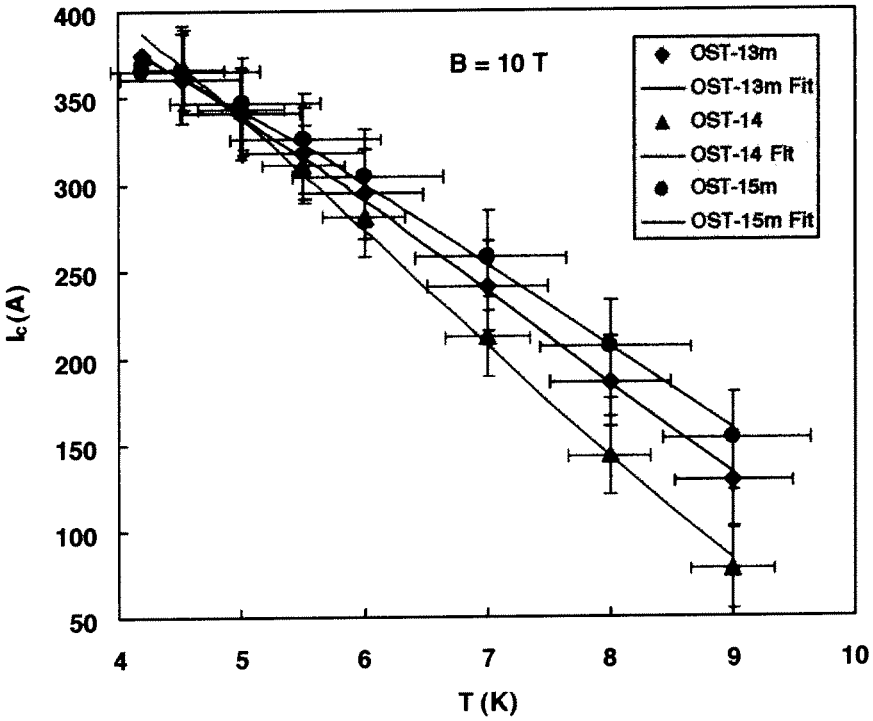

Figure 3-18. Scatter in the critical currents of OST-13 (modified set-up), OST-14 (with silicon paste), and OST-15 (modified set-up). The error bars, listed in Table 3-3, are also shown.

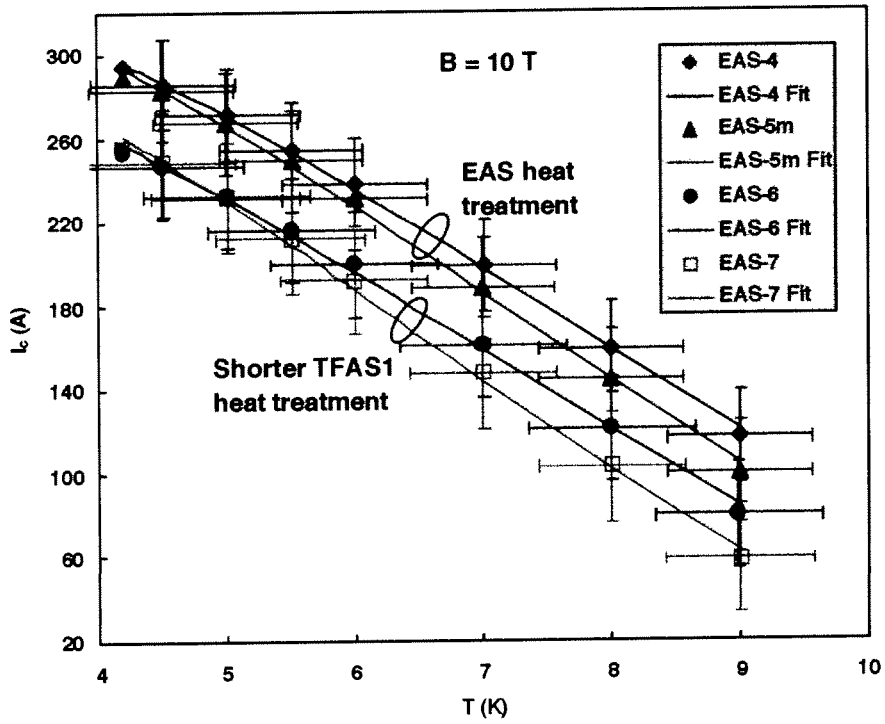

Figure 3-19. Scatter in the EAS critical current data for the long (EAS-4 and EAS-5) and the TFAS1 heat treatment (EAS-6 and EAS-7). The error bars, listed in Table 3-3, are also shown.

The scatter of the data within each of the two groups of EAS specimens, distinguished only by different heat treatments, are for all temperatures smaller than the sum of the corresponding error bars. The data, shown in Figures 3-18 and 3-19, suggest that the data listed in Tables 3-1, 3-2, and 3-3 provide a reasonable estimate of the uncertainty of the measured critical current at elevated temperatures. In spite of the large systematic errors in the strand temperature the measured I_c data provide a rough estimate of the field and temperature dependencies of the critical current of the investigated strands. For most of the measurements the estimated error in I_c is around 25 A.

Figures 3-20, 3-21, 3-22, 3-23, and 3-24 show the critical current of OST-13, EAS-3 (long heat treatment), EAS-6 (TFAS1 heat treatment), OCSI, and OKSC-6, respectively, as a function of temperature and field. The estimated error bars for strand temperature and critical current are also included in the figures. The fit lines are based on the Summers scaling laws (Equations (5) and (6)). In addition, the Summers fit lines for the minimum and maximum $T_c(\varepsilon)$ values, found from the K- and B_{c2}-fits, have been also calculated and included in the figures.

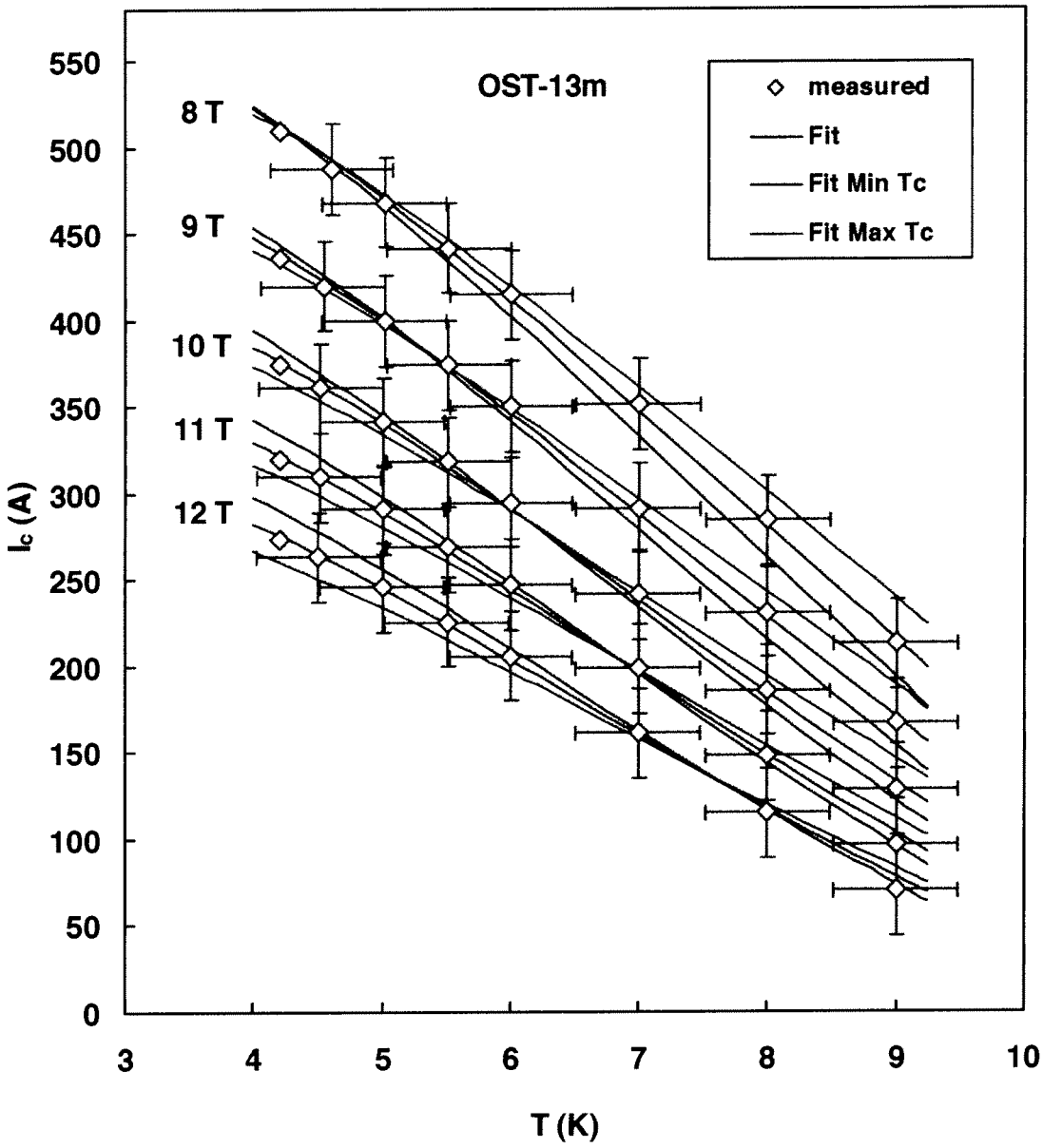

Figure 3-20. Critical current of OST-13 as a function of temperature for fields between 8 and 12 T. The measurements have been performed in the modified set-up.

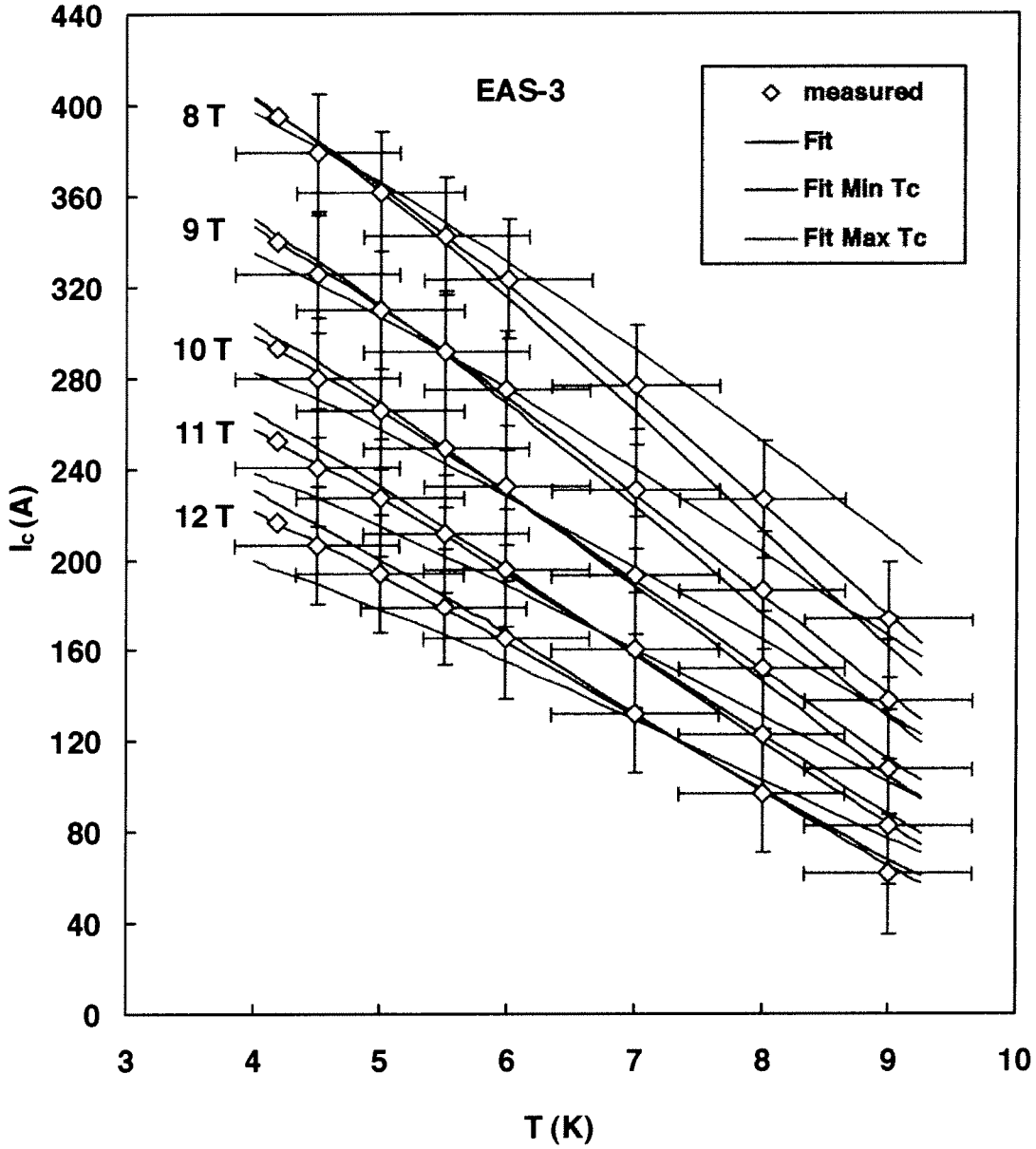

Figure 3-21. Critical current of EAS-3 as a function of temperature for fields between 8 and 12 T (measurements with silicon paste). The long heat treatment has been used for EAS-3.

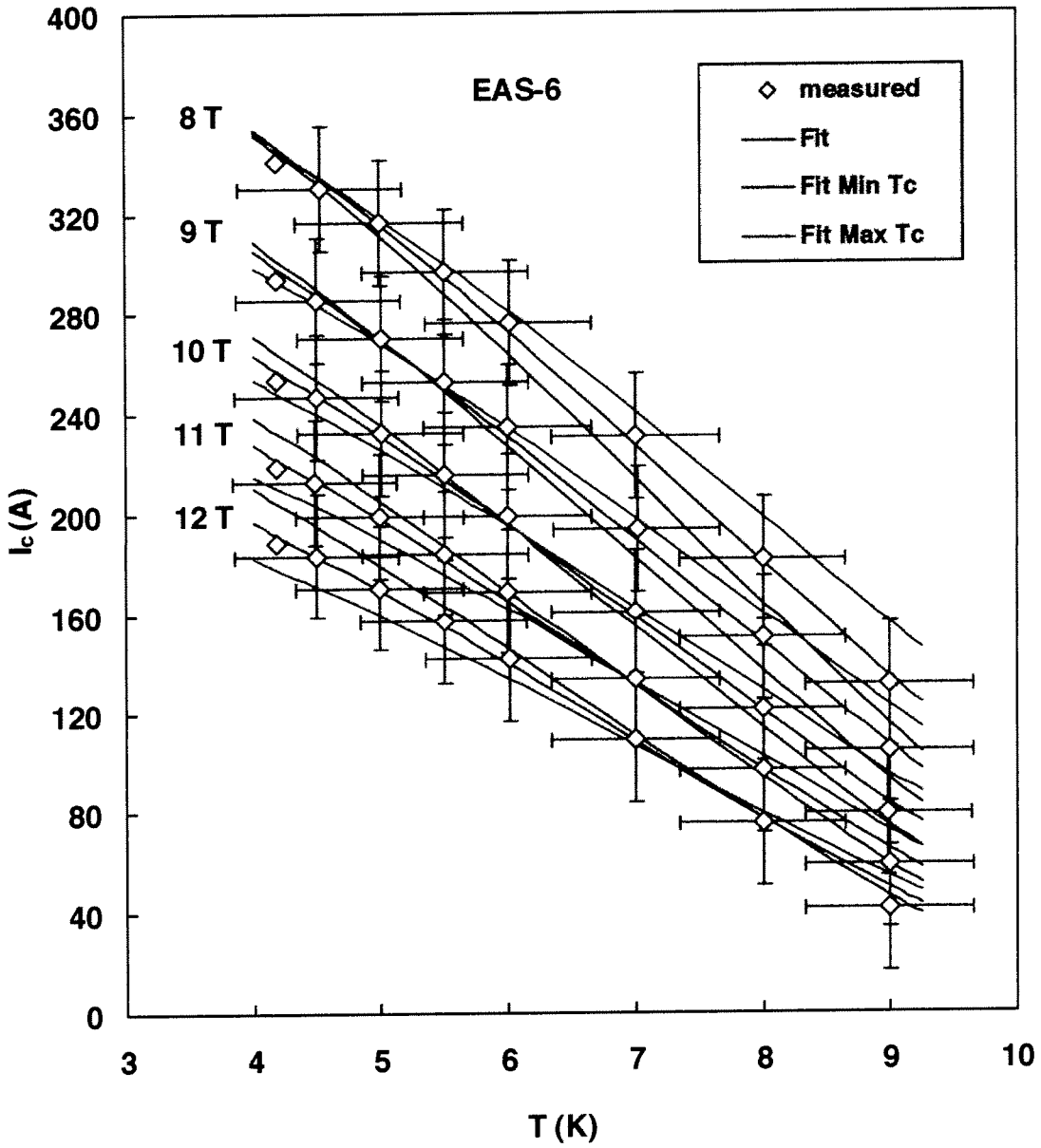

Figure 3-22. Critical current of EAS-6 as a function of temperature for fields between 8 and 12 T (measurements with silicon paste). The specimen has been heat treated together with the TFAS1 conductor.

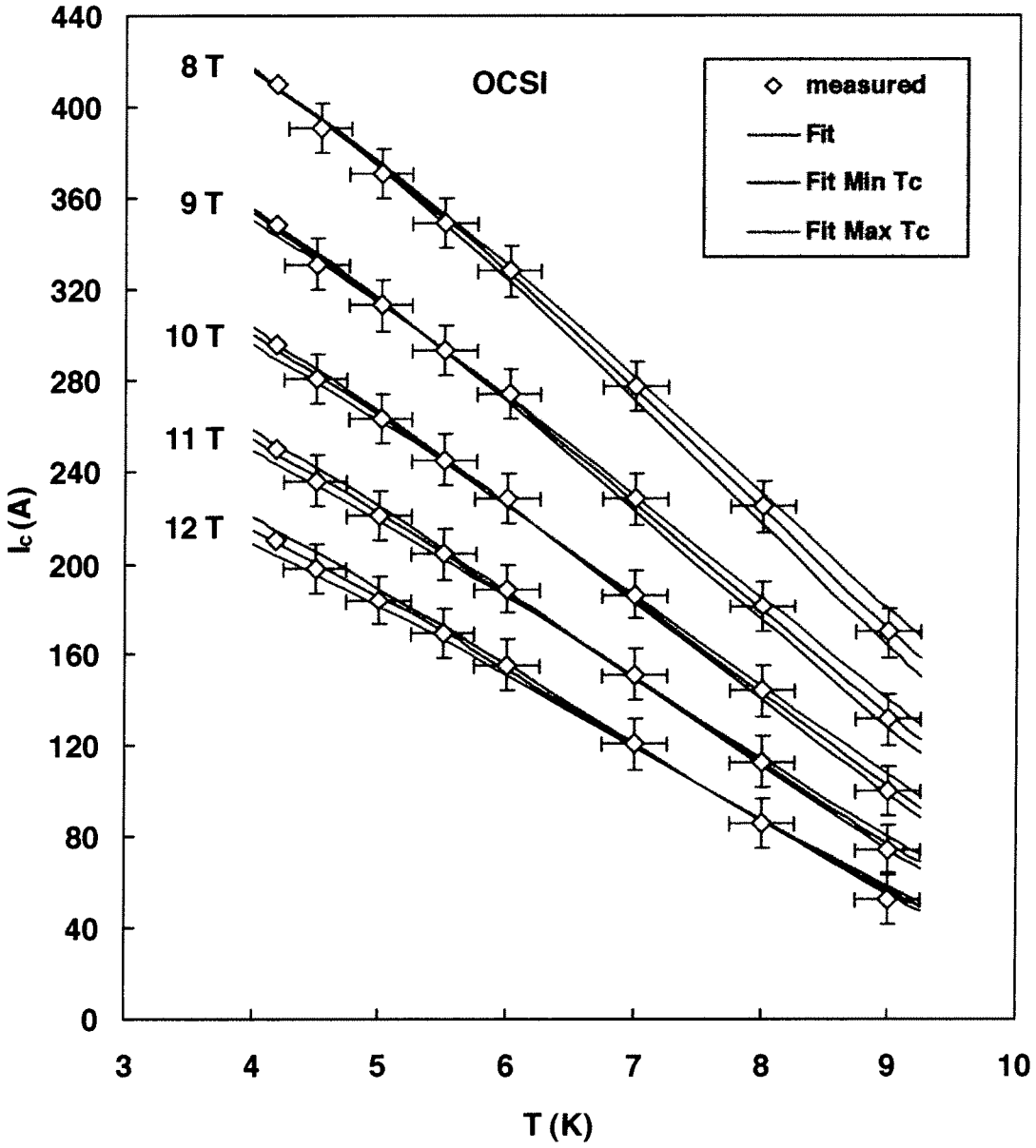

Figure 3-23. Average critical current of OCSI-1, 2, and 3 as a function of temperature for fields between 8 and 12 T. The measurements have been performed in the modified set-up.

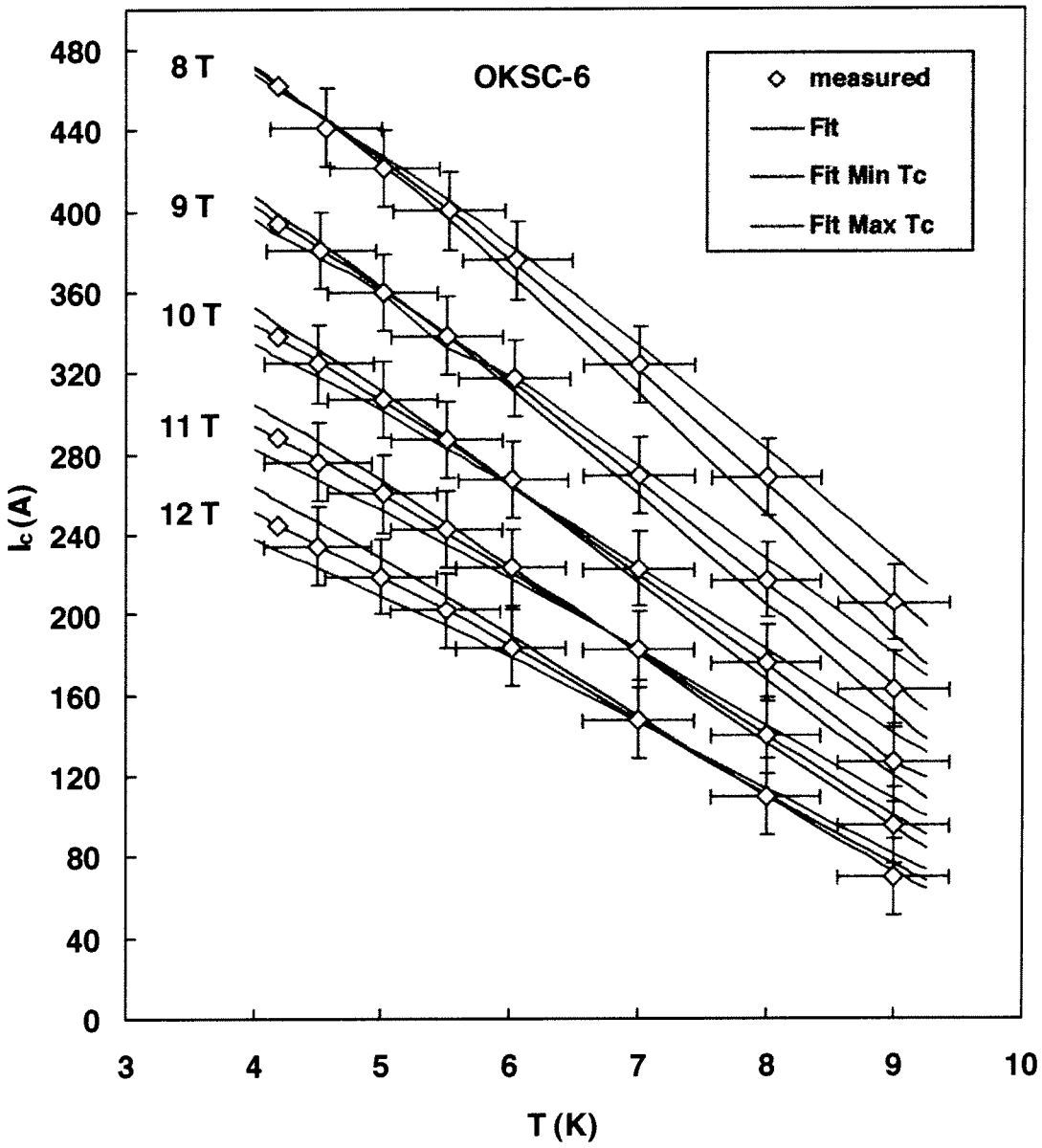

Figure 3-24. Critical current of OKSC-6 as a function of temperature for fields between 8 and 12 T. The measurements have been performed in the modified set-up.

3.3 Voltage-Current Characteristic

The n factors, defined by the power law $E = E_c(I/I_c)^n$, have been determined in the electric field range of 0.1 to 1 μV/cm for the measurements performed in liquid helium. For the measurements, performed in the temperature variable cryostat, the take-off electric field is typically smaller than 1 μV/cm. To have a sufficiently large range in the electric field a lower boundary between 0.04 and 0.08 μV/cm has been used in the determination of the n value. Measurements at nominal temperatures of 4.5 K provide overestimated n values because of the temperature increase during the transition. At higher temperatures this effect is negligible. Therefore, the 4.5 K data have been generally omitted. In the case of the OST strands even the n values at 5 K are strongly overestimated and need to be omitted. In the present report the n factors are always shown as a function of the critical current. The systematic error in the strand temperature is therefore of no importance.

Figure 3-25 (left) shows the n values of OST-13, 14, and 15 as a function of the critical current. The scatter in the n values of the different specimens is moderate. The n values of all three OST specimens have been used for a fit to the expression $n(J_c) = 1 + a\,J_c^b$ (J_c in A/mm^2). The result of the fit is shown in Figure 3-25 (right). The corresponding data for the EAS strands are shown in Figures 3-26 (long heat treatment) and in Figure 3-27 (TFAS1 heat treatment).

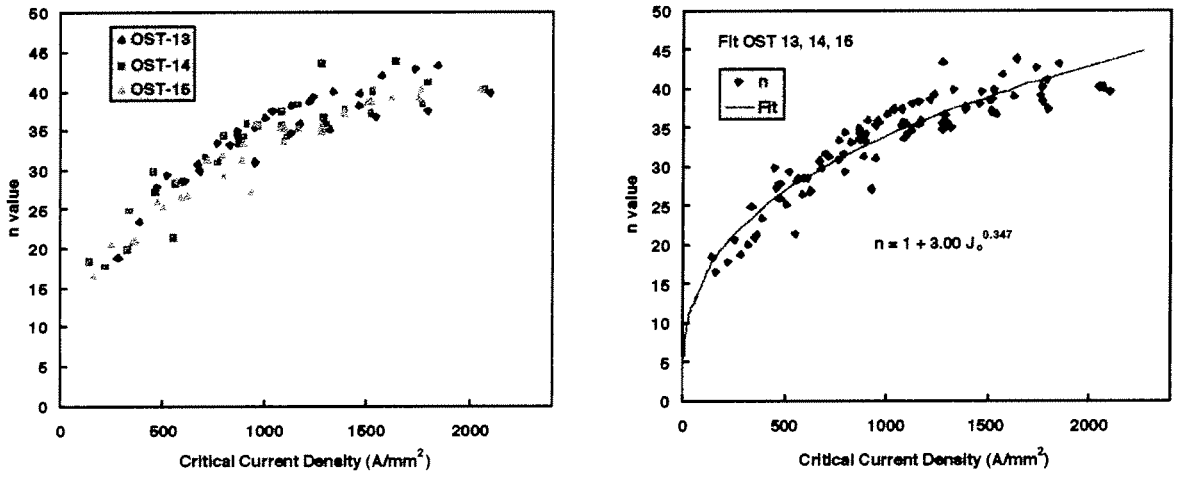

Figure 3-25. The n values of OST-13, 14, and 15 as a function of the critical current density (left). A fit of the expression $n(J_c) = 1 + a\,J_c^b$ to the data is shown on the right.

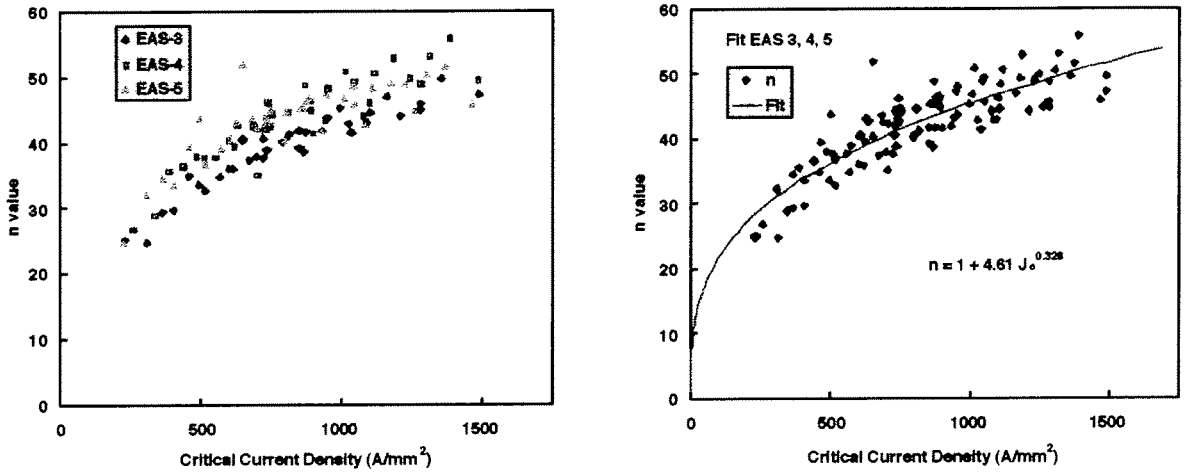

Figure 3-26. The n values of EAS-3, 4, and 5 (long heat treatment) as a function of the critical current density (left). A fit of the expression $n(J_c) = 1 + a\,J_c^{\,b}$ to the data is shown on the right.

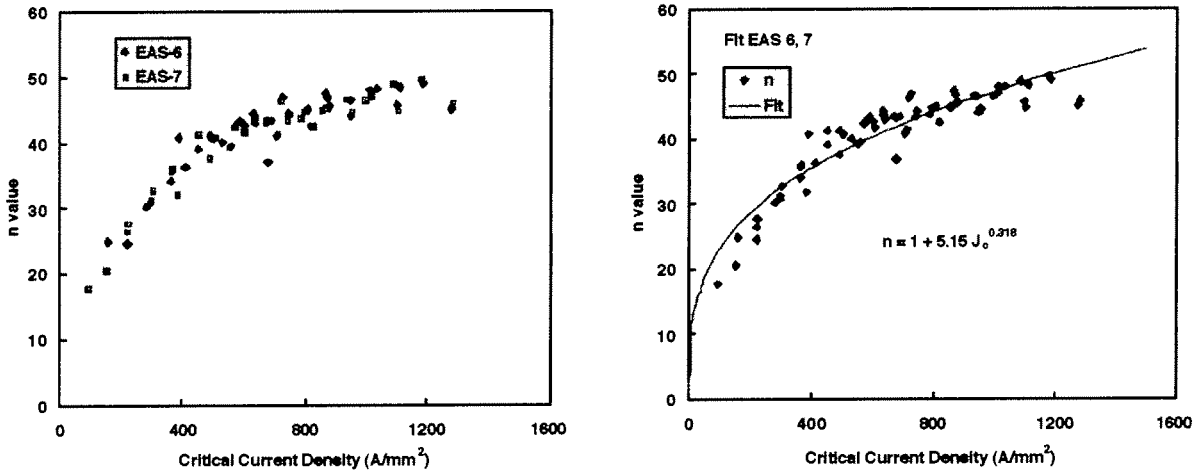

Figure 3-27. The n values of EAS-6 and 7 (TFAS1 heat treatment) as a function of the critical current density (left). A fit of the expression $n(J_c) = 1 + a\,J_c^{\,b}$ to the data is shown on the right.

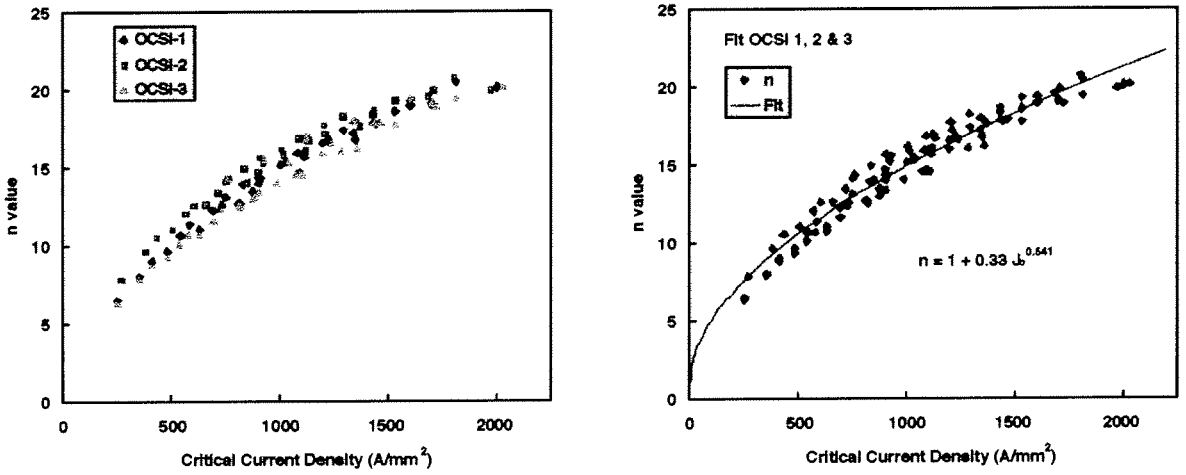

Figure 3-28. The n values of OCSI-1, 2, and 3 as a function of the critical current density (left). A fit of the expression $n(J_c) = 1 + a J_c^b$ to the data is shown on the right.

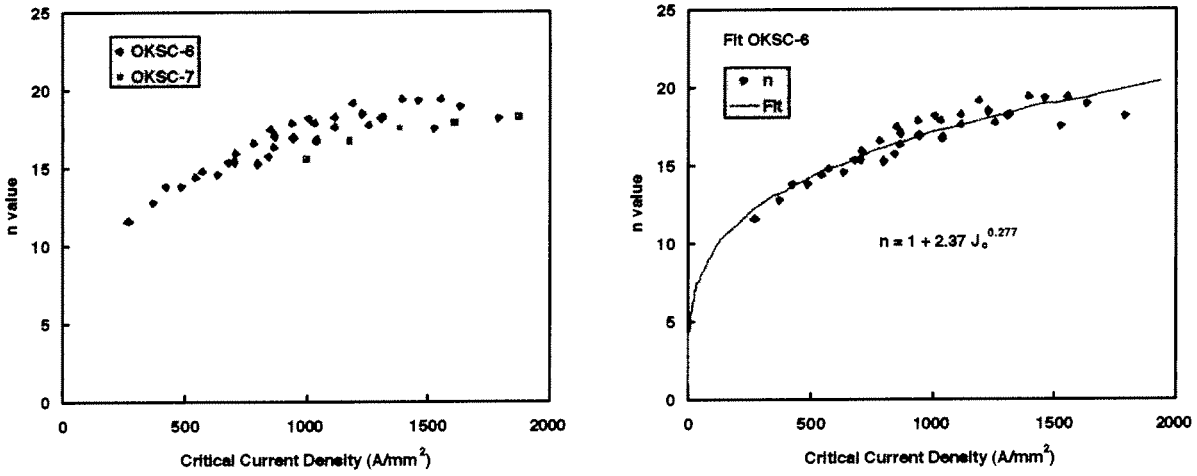

Figure 3-29. The n values of OKSC-6 and 7 as a function of the critical current density (left). A fit of the expression $n(J_c) = 1 + a J_c^b$ to the n values of OKSC-6 is shown on the right.

4. Summary

The main results of the strand measurements, performed at CRPP, are summarised in Table 4-1. The Cu : non-Cu ratios, determined by an etching and weighing procedure are close to the values provided by the manufacturers. The critical current of the OST-7845 strands at 4.2 K and 12 T is slightly below the expectations. The lower critical current may be the consequence of a larger Cu : non-Cu ratio. The non-copper critical current densities for the OST-7845, EAS (long heat treatment), OCSI, and OKSC advanced strands at 4.2 K and 12 T are 1104, 808, 1029 and 974 A/mm^2, respectively. The n values at 4.2 K and 12 T are extremely high for the OST (n = 34) and the EAS advanced strands (n = 41). On the other hand, a relatively low n value of 16 (4.2 K, 12 T) has been found for the other two advanced strands. The residual resistivity ratio (*RRR*) is well above 200 for strands heat treated without the chromium coating. Strongly reduced *RRR* values have been found for the strands heat treated with the chromium coating. This result suggests that the copper stabiliser is slightly poisoned by in-diffusion of chromium leading to *RRR* values between 95 and 130. The Kramer upper critical fields for the OST-7845, EAS (long heat treatment), OCSI, and OKSC advanced strands at 4.2 K are 28.86, 29.94, 27.35, and 28.76 T, respectively. The highest upper critical field at 4.2 K has been found for the EAS strand.

Table 4-1. DC performance of the advanced strands.

Strand	d (mm)	Cu:non-Cu	*RRR*	I_c(4.2 K, 12 T) (A)	n (4.2 K, 12 T)	B_{c2}(4.2 K) (T)[1]
OST-7845 #13, 14, 15	0.81	1.12[2]	285[3] 130[4]	268.4[5]	34[6]	28.86[6]
OST-7878 #16, 17	0.81	-	-	276.0[7]	34[6]	-
EAS-A1-8930[8] #3, 4, 5	0.81	0.93[9]	230[3] 95[4]	215.7[10]	41[10]	29.94[10]
EAS-A1-8930[8] #6, 7	0.81	0.93[9]	230[3] 95[4]	189.2[11]	41[12]	30.76[12]
OCSI #1, 2, 3	0.81	1.52[13]	240[3][15] 95[4]	210.5[6]	16[6]	27.35[6]
OKSC #6, 7	0.81	-	-	251.0[14]	16[6]	28.76[6]

[1] Derived from the Kramer plots
[2] 1.0-1.05 with a possible variation of 0.05 (OST) [5]
[3] Without chromium coating
[4] With chromium coating
[5] Average value, TFAS1 heat treatment, 278 A (OST) [5], 275 A (ENEA) [5]
[6] Average values
[7] Average value, TFAS1 heat treatment, 273-278 A (OST) [5]
[8] NSTT 8305-HK002-A1
[9] 0.92 (EAS) [5]
[10] Average value, long heat treatment
[11] Average value, TFAS1 heat treatment, 188-190 A (FZK) [5]
[12] Average value, TFAS1 heat treatment
[13] 1.45 (OCSI) [5]
[14] Average value, 270 A (Durham University, other billet) [5], 235 A (CEA, however problems during the heat treatment) [5]
[15] Large scatter in the data

In general, the dependence of the n values on the critical current can be well represented by the expression $n(J_c) = 1 + a\, J_c^b$, where the critical current is in A. The scaling parameters are listed in Table 4-2.

Table 4-2. Scaling parameters for the dependence of the n value on the critical current.

Strand	a	b	Comments
OST-7845 (#13, 14, 15)	3.00	0.347	TFAS1 heat treatment
EAS-A1-8930 (#3, 4, 5)	4.61	0.328	Long heat treatment
EAS-A1-8930 (#6, 7)	5.15	0.318	TFAS1 heat treatment
OCSI (#1, 2, 3)	0.33	0.541	TFAS2 heat treatment
OKSC (#6, 7)	2.37	0.277	TFAS2 heat treatment

The average values of $T_c(\varepsilon)$, $B_{c20}(\varepsilon)$, and $C(\varepsilon)$, obtained from the Summers fits are listed in Table 43. Please note that the values quoted in Table 3-6 may be considered as a rough estimate because of systematic errors in the strand temperature.

Table 4-3. Scaling parameters estimated from the Summers fits.

Strand	$T_c(\varepsilon)$ (K)	$B_{c20}(\varepsilon)$ (T)	$C(\varepsilon)$ $AT^{1/2}$	Comments
OST-7845 (#13, 14, 15)	17.02	33.39	3158	TFAS1 heat treatment
EAS-A1-8930 (#3, 4, 5)	17.93	33.69	2350	Long heat treatment
EAS-A1-8930 (#6, 7)	16.07	35.52	2079	TFAS1 heat treatment
OCSI (#1, 2, 3)	17.90	30.72	2591	TFAS2 heat treatment
OKSC (#6, 7)	18.25	32.03	2815	TFAS2 heat treatment

The presently available $I_c(B,T)$ apparatus needs to be improved to allow us the measurement of critical currents well above 300 A. The heat generation in the current leads and the contacts has to be reduced providing the possibility to measure the critical current at considerably reduced helium gas pressures. In addition, an improved thermal contact of the strand under test and the ITER barrel is required. This may be achieved by the use of Stycast epoxy. Finally, a variation of the gas pressure for different current and temperature levels may be necessary (i.e. low pressure at high temperatures and low currents).

5. Acknowledgement

This work has been performed in the frame of the European Fusion Technology Programme under Task EFDA ASTEST Contract 03-1121. The technical support of the Paul Scherrer Institute PSI is greatly acknowledged.

6. References

1. J. D. Verhoeven, K. Heimes, and A. Efron, *Analysis of the tin diffusion step in Nb_3Sn-Cu superconducting wire produced by external tin process,* **J. Appl. Phys. 59** (1986) 2096.

2. H. Benz, I. Horvath, K. Kwasnitza, R. K. Maix, and G. Meyer, *Worldwide cryogenics-Switzerland, Cryogenics at BBC Brown, Boveri and Co,* **Cryogenics 19** (1979) 435.

3. M. Hansen, *Constitution of binary alloys,* 2nd ed., McGraw-Hill, New York (1958) p. 633.

4. B. L. Brandt, D. W. Liu, and L. G. Rubin, *Low temperature thermometry in high magnetic fields. VII. Cernox™ sensors to 32 T,* **Review of Scientific Instruments 70** (1999) 104.

5. A. Vostner, private communication

6. E. J. Kramer, *Scaling laws for flux pinning in hard superconductors,* **J. Appl. Phys. 44** (1973) 1360.

7. L. T. Summers, M. W. Guinan, J. R. Miller, and P. A. Hahn, *A model for the prediction of Nb_3Sn critical current as a function of field, temperature, strain, and radiation damage,* **IEEE Trans. Magn. 27** (1991) 2041.